RESEARCH ARTICLE

VOLCANICA

Degassing-induced chemical heterogeneity at the 2011–2012 Cordón Caulle eruption

Rebecca Paisley*[α], Kim Berlo[α], Jack Whattam[β], C. Ian Schipper[β], Hugh Tuffen[γ]

[α] *Department of Earth Planetary Sciences, McGill University, 3450 Rue University, Montreal, Quebec, H3A 0E8, Canada*
[β] *School of Geography, Environment and Earth Sciences, Victoria University, PO Box 600, Wellington 6140, New Zealand*
[γ] *Lancaster Environment Centre, Lancaster University, LA1 4YQ, UK*

Abstract

The mechanisms of hazardous rhyolitic eruptions such as Cordón Caulle, Chile, in 2011–2012 are controlled by poorly-understood shallow conduit processes. Here we characterise texturally and chemically heterogeneous domains (e.g. ash, breccias and tuffisites) generated via fracturing, gas fluxing and melt relaxation within the conduit, and preserved in glassy, oxidised and devitrified samples. Volatile trace element depletions (e.g. Zn, Pb) in relict degassing pathways record metal scavenging by fluxing gases. Diffusion modelling of preserved trace element concentration gradients (e.g. Li, Rb, Tl) at domain interfaces indicate deep-conduit degassing events were short-lived (~minutes) whereas late-stage venting from discrete locations was prolonged (~hours), corroborating visual observations of the eruption. Later-erupted vent deposits are volatile-depleted with respect to earlier-erupted bombs, indicating progressive syn-eruptive volatile loss. We show that a combination of *in situ* textural and volatile trace element analyses can provide new constraints on magmatic degassing in shallow systems depleted in H_2O and CO_2.

Résumé

Les éruptions dangereuses de type rhyolitiques comme l'éruption du Cordón Caulle, au Chili, en 2011–2012, sont contrôlés par des mécanismes mal compris qui sont localisés dans un conduit peu profond. Dans cette étude, nous caractérisons des domaines où la texture et la chimie sont hétérogènes (par exemple : les cendres, les brèches et les tuffisite). Ces domaines ont été généré par la fracturation, le flux de gaz et la relaxation du liquide dans le conduit et sont conservées dans des échantillons vitreux, oxydés et dévitrifiés. L'appauvrissement des éléments traces et volatiles (par exemple Zn, Pb) enregistré dans les voies de dégazage, témoigne de l'absorption du métal par le flux de gaz. La modélisation des gradients de diffusion des éléments traces conservés (par exemple, Li, Rb, Tl) aux interfaces des domaines, indiquent que des événements de dégazage en conduit profond ont été de courte durée (~minutes) alors que la ventilation tardive de zones plus localisées était de longue durée (~heures). Ces résultats sont en accord avec des observations visuelles de l'éruption. Les dépôts tardifs sont appauvris en volatiles par rapport aux bombes éjectés antérieurement. Cela indique une perte en volatile progressive durant l'éruptive. Nous montrons qu'une association d'analyses in situ des textures et des éléments traces volatiles peut fournir de nouvelles contraintes sur le dégazage magmatique dans des systèmes peu profonds et appauvris en H_2O et CO_2.

Keywords: Degassing; Rhyolite volcanism; Cordón Caulle; Trace element diffusion; Magma fracturing

1 Introduction

Prior to the 2008–2009 eruption of Chaitén in Chile, no explosive rhyolitic eruptions had been visually observed by scientists [Castro et al. 2014]. The Chaitén eruption was closely followed by another Chilean rhyolitic eruption at Cordón Caulle from 2011 to 2012. During both eruptions simultaneous explosive and effusive activity from the same vent was observed, known as "hybrid" activity [Pallister et al. 2013; Schipper et al. 2013]. Observations of hybrid activity have led to a paradigm shift in our understanding of syn-eruptive degassing of silicic magma and highlight the important role played by melt fracturing in the upper conduit. Such fracturing processes are recorded by tuffisite veins, which are ash-filled fractures formed in shallow magma or country rock and found in the products of many silicic eruptions [e.g. Heiken et al. 1988; Stasiuk et al. 1996; Tuffen and Dingwell 2005; Tuffen et al. 2003], and by variably-welded breccias [e.g. Isgett et al. 2017; Kolzenburg and Russell 2014]. Geochemi-

*Corresponding author: rebecca.paisley@mail.mcgill.ca

cal, textural and experimental studies have shown fractures to be highly permeable, transient pathways where volcanic gases can flux over hundreds of metres within the upper conduit, before sintering and compaction leads to porosity and permeability loss that stifles gas flow [e.g. Farquharson et al. 2016; Heap et al. 2015; Kendrick et al. 2016; Kolzenburg et al. 2012; Saubin et al. 2016]. H_2O diffusion gradients in glasses have been used to constrain the timescale of degassing into fractures at Chaitén [Castro et al. 2012], Lipari [Cabrera et al. 2011] and Mono Craters [Watkins et al. 2017]. However, the erupted products from Cordón Caulle are H_2O-poor (<0.35 wt.% H_2O) and lack well-defined degassing trends in both water concentrations and isotopes [Castro et al. 2014; Schipper et al. 2013]. Therefore, alternative approaches are required to chemically constrain degassing processes during eruptions that produce texturally complex but extensively degassed erupted products.

Whilst volcanic vapour compositions are dominated by H_2O, CO_2, sulphur and halogens, they are also enriched in trace elements including alkalis, metals and metalloids [Hinkley et al. 1994; Symonds et al. 1987; Williams-Jones et al. 2002]. Trace element variations in tuffisites have been linked to gas fluxing through these permeable pathways at depth [Berlo et al. 2013; Paisley et al. 2019; Plail et al. 2014]. As their diffusivities are commonly slower than that of H_2O [Gardner et al. 2012; Zhang and Ni 2010; Zhang et al. 2010], heterogeneity in certain trace elements may be recorded spatially, and this can be exploited to reconstruct degassing systematics and timescales. In this study, we exploit the differences in diffusivities and evaluate heterogeneity in volatile trace elements (e.g. Li, Rb, Cs, Cu, Tl, Pb) and ligands (e.g. Cl) across textural features indicative of degassing preserved in the erupted products from the most recent Cordón Caulle eruption.

2 Case Study: The Puyehue-Cordón Caulle Volcanic Complex

2.1 Summary of the 2011–2012 eruption

The Puyehue–Cordón Caulle Volcanic complex (PCCVC) is located in the Chilean Southern Volcanic Zone (SVZ). Historical eruptions on the complex range from basaltic to rhyolitic in composition [Gerlach et al. 1988]. The Cordón Caulle fissure system is located within a NW–SE oriented graben, between the Puyehue composite stratovolcano (~2230 m a.s.l) and the Cordillera Nevada caldera (~1800 m a.s.l), and is controlled by a branching fault off-shooting from the 1000+ km-long, N–S striking Liquiñe-Ofqui Fault Zone in the SVZ [Gerlach et al. 1988; Lara et al. 2006; Singer et al. 2008]. Prior to the 2011–12 eruption, the two most recent eruptions of the Cordón Caulle fissure zone in 1922 and 1960 were rhyodacitic to rhyolitic in composition [Gerlach et al. 1988], with the latter notably occurring 38 hours after the M_w 9.5 Valdivia subduction zone earthquake, the largest instrumentally recorded seismic event [Lara et al. 2004].

The 2011–2012 eruption commenced on June 4th with 27 hours of Plinian activity after months of elevated seismicity, ground deformation and uplift [Jay et al. 2014; Silva Parejas et al. 2012]. The column height was initially 15 km, before fluctuating between 3 and 10 km over the next 7 to 9 days [Castro et al. 2013; Silva Parejas et al. 2012, and references therein]. Ballistic bomb emplacement around the vent area began June 7th [Pistolesi et al. 2015]. Lava effusion began ~ten days into the eruption (~June 15th), from the same vents as the pyroclastic emissions, accompanied by breaching of the northwest side of the tephra cone [Schipper et al. 2013; Silva Parejas et al. 2012]. Rapid surface uplift of up to 200 m around the vent is thought to indicate the emplacement of a ~0.8 km^3 laccolithic intrusion, at a depth of 20–200 m, in the first month of the eruption [Castro et al. 2016]. Pyroclastic emissions continued for almost ten months, with the concurrent coalescence of two partly-overlapping cones formed in the early stages of eruption. In January 2012 two sub-vents within a single tephra cone were observed, each displaying a cycle of behaviour from Vulcanian blasting (with bombs landing <1 km away from the vent) to ash and gas venting [Schipper et al. 2013; Silva Parejas et al. 2012]. This hybrid behaviour continued into 2012, when recorded tremor ceased, after emission of a total erupted volume of magma of ~1.4 km^3 dense rock equivalent [Pistolesi et al. 2015; SERNAGEOMIN/OVDAS 2012; Tuffen et al. 2013]. The lava effusion rate averaged 50 m^{3}s^{-1} during the first 20 days before declining to lower fluxes, and the 35 m-thick lava flow continued to advance via breakouts from its thermally-insulated core into 2013 [Bertin et al. 2015; Magnall et al. 2018; Tuffen et al. 2013]. Extensive deformation was also recorded post eruption [Delgado et al. 2016].

2.2 Petrological summary of the 2011–2012 eruption

Bulk SiO_2 (69 wt.%) and glass (72 wt.%) concentrations from the 2011–2012 eruption show minimal variation across the eruption suite and are comparable to the 1922 and 1960 eruptions at Cordón Caulle [Castro et al. 2013; Gerlach et al. 1988; Pistolesi et al. 2015]. Phenocryst growth occurring during magma storage accounts for the minor difference between the bulk and glass compositions [Castro et al. 2013]. The most recent magmas form an extended trend in both major and trace elements when compared to historical bulk analyses of the PCCVC glacial and post-glacial deposits, which is thought to result from fractional crystallisation of an anhydrous assemblage of plagioclase, clinopyroxene, orthopyroxene and magnetite [Alloway et al. 2015; Castro et al. 2013; Daga et al. 2014; Gerlach et al. 1988; Jicha et al. 2007].

The 2011–2012 phenocryst assemblage comprises of plagioclase, orthopyroxene, clinopyroxene, magnetite and ilmenite with rare apatite and pyrrhotite, although samples are near aphyric (<5 vol. %) and crystals are commonly observed as glomerocrysts [Castro et al. 2013]. Minor volumes of mafic magma, preserved as crystal-rich, vesiculated enclaves, co-erupted with the rhyolitic melt [Ruprecht and Winslow 2017]. Magmatic storage conditions for this eruption are estimated to be ~2.5–7.5 km deep with a temperature of 875–925 °C and fO_2 close to the quartz-fayalite-magnetite (QFM) redox buffer assemblage [Castro et al. 2013; Jay et al. 2014]. Plagioclase-hosted melt inclusions record pre-eruptive volatile concentrations of <2.5 wt.% H_2O, and ~40–70 ppm CO_2 [Castro et al. 2013], whilst pyroxene-hosted inclusions contain ~3.9 wt.% H_2O, ~220 ppm CO_2 and ~130 ppm SO_2 [Jay et al. 2014]. The groundmass of the erupted products from the 2011 event is uniformly low in H_2O (<0.35 wt.%), with no systematic differences in H_2O or δD between the products of various eruptive phases (e.g. Plinian pumice, Vulcanian bombs, and lava [Castro et al. 2014; Schipper et al. 2013]). Thus less is known about magmatic degassing at Cordón Caulle than other eruptions that have ejected more deeply excavated, H_2O-richer, pyroclasts, for example the 2008–2009 Chaitén eruption [Forte and Castro 2019].

3 Methods

3.1 Sampling Methods

To accurately assess degassing processes during the 2011–2012 Cordón Caulle eruption samples must represent degassing events both through time (beginning to end) and space (from depth to the surface). This allows for an understanding of how volatiles degas as magma ascends from depth, and how degassing processes changed in an eruption that was initially explosive then transitioned into prolonged hybrid behaviour. To achieve this, relevant samples were collected that encapsulate shifting degassing systematics from the onset of ballistic ejections to the end of the hybrid phase of activity. They are subdivided into three categories: *bomb*, *vent* and *flow*. Figure 1 summarises sample collection localities and the phases of hybrid activity they represent. *Bomb* samples were predominantly collected from ballistic ejecta mantling a ridge ~2.5 km NW of the vent. Observations of the eruption note these were ejected during the lower intensity explosive phase (beginning June 7th) and during the onset of vigorous hybrid activity approximately a week later [Pistolesi et al. 2015; Schipper et al. 2013]. Further *bomb* samples were collected near or in the vent complex within the tephra cone, and these are bombs or bomb fragments that were ejected later during the eruption when many lower energy explosions had ballistic ejecta fail to escape the crater within the tephra cone [Schipper et al. 2013]. *Vent* samples are those collected exclusively from within the vent, with many sampled *in situ*, and represent the surfaces of fractures within the vent-filling lava (sub-vents of Schipper et al. [2013]) that acted as loci for ash and gas emissions during the waning phases of the hybrid activity in 2012. Material representing earlier vent processes has been incorporated into the moving flow and was inaccessible when sampling took place. *Flow* samples are collected from the rhyolite flow, with samples from the flow front of the northern branch likely representing the first-effused lava from the onset of the hybrid phase (June 2011), and the sample from within the vent representing the very end of activity in 2012 [Magnall et al. 2017; Magnall et al. 2018].

During explosive eruptions, degassing starts deep within the system with the exsolution of volatiles and continues all the way to the surface with the emission of a plume [Cashman and Sparks 2013]. Samples are subdivided into textural domains that reflect degassing processes within specific regions of the upper conduit and surface environment, and are summarised in Subsection 4.1 and Figure 2, with the underlying rationale discussed below. The collected samples represent surface and sub-surface degassing events. Surface degassing is recorded by *in situ* vent outcrops or material adhered to bomb surfaces. Sub-surface degassing domains are those that underwent fragmentation followed by varying degrees of melt relaxation, ductile deformation, welding and compaction (e.g. tuffisites, breccias and banded obsidians). These textures are known to be generated within the upper conduit and relate to outgassing [e.g. Farquharson et al. 2016; Gonnermann and Manga 2005; Isgett et al. 2017; Stasiuk et al. 1996; Tuffen and Dingwell 2005; Tuffen et al. 2003]. Flow textures are not discussed in this study as the rhyolite flow undergoes additional processes at the surface as it cools that are recorded texturally and chemically, e.g. devitrification, second boiling and continued outgassing [Magnall et al. 2018; Schipper et al. 2015; Schipper et al. 2019].

3.2 Analytical Methods

Geochemical analyses were performed on polished thin sections (30–50 µm thick) and one-inch mounts both made from epoxy-impregnated samples. Electron probe microanalysis (EPMA) was conducted on the JEOL JXA-8230 at Victoria University of Wellington. Each spot was analysed twice, once for SiO_2, TiO_2, Al_2O_3, FeO, MnO, MgO, CaO, Na_2O, K_2O, Cr_2O_3 and P_2O_5, and secondly for S and Cl. Defocused beam sizes of 10–20 µm were used with working conditions of 15 kV and 8.0 nA for major elements and 15 kV and 60.0 nA for volatile elements. Counting times for major elements were 30 and 15 seconds (peak and background). Sodium loss was avoided by analysing Na_2O first at re-

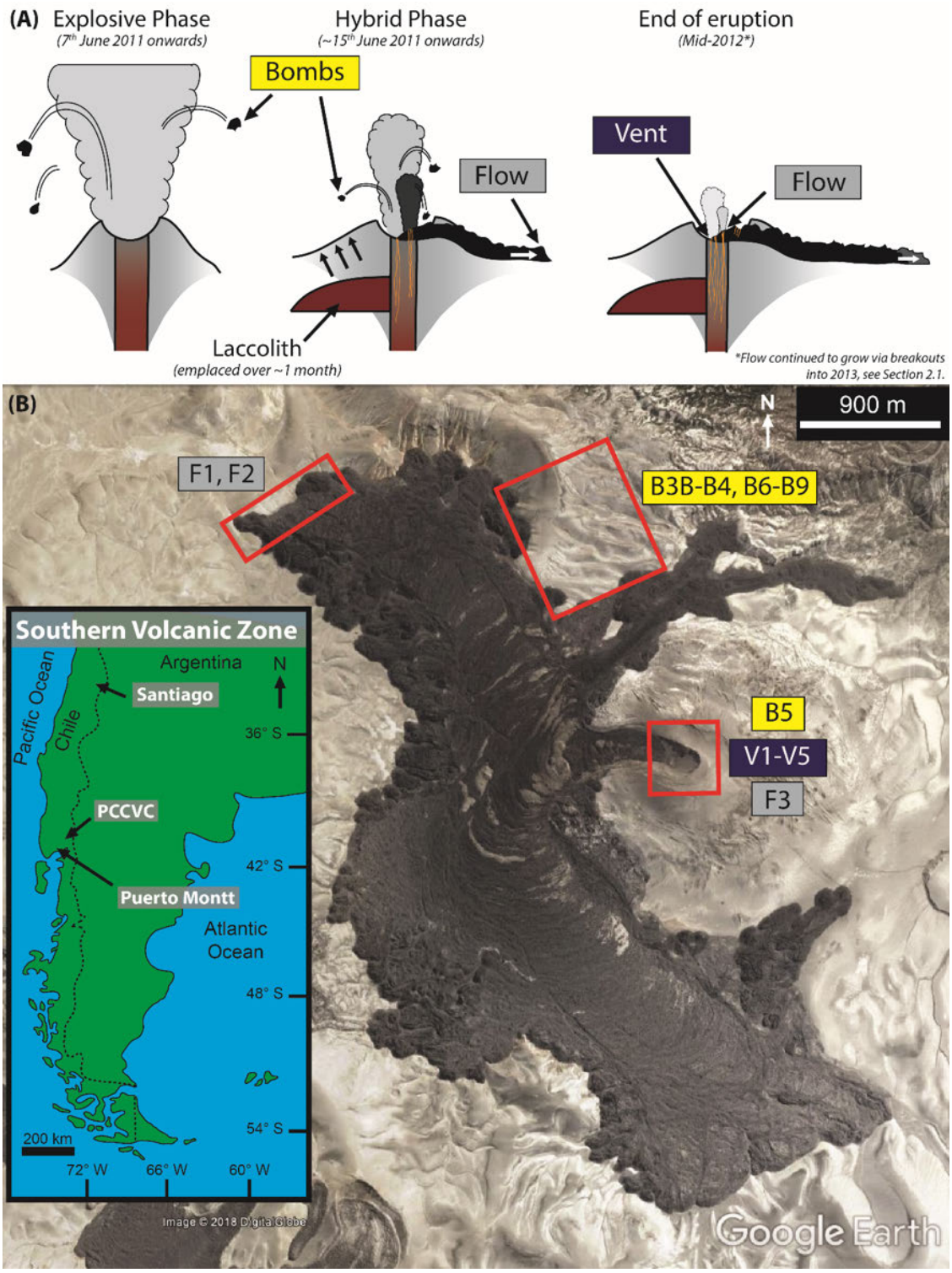

Figure 1: [A] Schematic timeline of eruption. Samples collected represent the explosive (*bombs*) and effusive (*flow*) components of the eruption and *vent* degassing processes. *Bomb* samples analysed were largely ejected earlier in the eruption when ballistics were observed to have been ejected over 2 km from the vent. Arrows indicate inflation associated with laccolith emplacement [Castro et al. 2016]. [B] Annotated Google Earth™ image of 2011–2012 Cordón Caulle flow, SVZ, Chile. © 2015 Google. Boxes (red) highlight collection localities of *bomb* samples (B3B–B9) from across the complex and *vent* samples (V1–V5) that were collected *in situ* and record later degassing processes. *Flow* material (F1 and F2) collected far from the vent represent the earlier effusive activity, F3 represents the last flow material to leave the conduit. [*Inset*]: location of PCCVC in context of the SVZ in Chile.

duced times of 10 and 5 seconds, with no peak search. Volatiles were measured for 60 and 30 seconds (peak and background). Cr_2O_3 and P_2O_5 were consistently below detection and are excluded. Iron is measured as total iron FeO_t. Primary standards were rhyolite glass VG568 for Si, Al, Na, K, and Cl; basaltic glass VGA99 for Ca, Mg, and Fe; pure synthetic oxides for Ti, Mn, and Cr; Elba Pyrite for S, and Durango apatite for P [Jarosewich et al. 1980]. Secondary standards (VG2, VGA99 and VG568) were periodically analysed to assess for drift during the analyses over several days. Relative standard deviations (% RSD) are calculated using these standards: SiO_2, Al_2O_3, and MgO (excluding values near detection limit) are <2 % RSD; TiO_2, CaO, FeO_t, Na_2O and K_2O are between 2 and 6 % RSD; % RSD is 7-8 % for Cl and 13–15 % for MnO. S is near detection in samples and has a % RSD <50. Crystals and void spaces were avoided to ensure a pure glass signature on the samples. Samples were further filtered for contamination by excluding data with low totals (due to void space) and anomalously high Al_2O_3, FeO_t, MgO and/or CaO (crystals), or Cl or S (resin) concentrations. Concentrations in Supplementary Material 1 are calculated anhydrous averages for each sample and reported as oxides except for Cl and S.

Laser ablation analyses were conducted using a NewWave 213 nm Nd-YAG laser ablation system coupled to a Thermo Finnigan iCapQ ICP-MS at McGill University, and a RESOlution S155-SE 193 nm Excimer Laser coupled to an Agilent 7500CS ICP-MS at Victoria University of Wellington. Spot sizes of 12–20 µm were used for laser profiles with a restricted element list, whilst large spots of 30–60 µm were used to analyse for a larger range of elements. Spot analyses, >30 µm in diameter, were randomly conducted on a thin section in multiple areas to ensure a representative mean concentration for a wide range of elements. Individual line analyses were conducted running parallel to interfaces to obtain data for diffusion profiles (Subsection 4.2.2). Analysis counting times (<45 seconds) for spot and line profiles were dependent on line length/spot size and thin section thickness. Each analysis was preceded by a single 70 or 140 µm cleaning pulse and a laser warm-up/background counting period of 30–45 seconds, followed by a <60 second washout period. Energy outputs and frequencies varied with spot size to ensure no melting or fracturing occurred during ablation. Analyses were conducted at 10–20 Hz with a resultant fluence of ~4–12 cm^{-2}. Up to 55 isotopes were analysed, including ^{7}Li, ^{23}Na, ^{24}Mg, ^{27}Al, ^{29}Si, ^{21}P, ^{39}K, ^{44}Ca, ^{45}Sc, ^{47}Ti, ^{51}V, ^{52}Cr, ^{55}Mn, ^{57}Fe, ^{59}Co, ^{60}Ni, ^{63}Cu, ^{66}Zn, ^{71}Ga, ^{75}As, ^{85}Rb, ^{88}Sr, ^{89}Y, ^{90}Zr, ^{93}Nb, ^{95}Mo, ^{107}Ag, ^{111}Cd, ^{115}In, ^{118}Sn, ^{121}Sb, ^{133}Cs, ^{137}Ba, ^{139}La, ^{140}Ce, ^{146}Nd, ^{147}Sm, ^{153}Eu, ^{157}Gd, ^{163}Dy, ^{166}Er, ^{172}Yb, ^{175}Lu, ^{178}Hf, ^{182}W, ^{205}Tl, ^{208}Pb, ^{232}Th, and ^{238}U. Na, Mg, Si, K, P, Ca, and Fe were measured to assess for crystal contamination, allowing contaminated spot analyses to be easily identified and removed from the dataset. Based on EPMA, Al was found to minimally vary in samples and a median concentration (14.1 wt. % Al_2O_3, interquartile range 14.0–14.3 wt.% Al_2O_3) is used for internal standardisation of the ICP-MS data. All laser analyses were bracketed by the primary standard NIST610 [Jochum et al. 2011], with BCR-2G repeatedly analysed as a secondary standard to assess for reproducibility and instrument precision. BCR-2G average elemental concentrations and associated % RSDs are noted in Supplementary Material 1. BCR-2G concentrations were compared to both the preferred GEOREM values [GeoReM 2009] and the median concentration of the wider selection of elements published values on GEOREM [published values GeoReM 2015]. Daily sessions were levelled using a robust regression calibration line calculated from the USGS standards GSC, GSD and GSE that were analysed at least twice per daily analytical session. Data reduction was undertaken in Iolite [Paton et al. 2011] with offline corrections for internal element standardisation. Further corrections were made to sessions that had systematically unusual BCR-2G concentrations. Errors on individual analyses are calculated by Iolite during processing and depend on the choice of integration window. Concentrations for each sample, Supplementary Material 1, are calculated means from all spot analyses conducted on a sample.

4 Results: Textural and Chemical Observations

4.1 Domain Petrology

Bomb and *vent* samples have complex and heterogeneous textures thought to preserve the fracturing and degassing events that melt undergoes within the conduit as it ascends from depth. Below we describe the main classifications of textural domains that constitute these samples. Each domain represents degassing processes within a distinct part of the conduit.

4.1.1 *Ash Domains*

Many bombs and bomb fragments found within the vent are partially coated in fine veneers of light pink-orange oxidised ash (Figure 2). This veneer commonly thickens in concave or uneven areas on bomb surfaces. Ash shards are <10 µm in size, and sub-millimetric laminations are defined by variations in grain size. The ash is glassy and largely devoid of microlites. Ash adheres to both non-oxidised and heavily oxidised and altered bomb surfaces. Ash domains are not preserved within samples, only on their surfaces.

4.1.2 *Nozzle Domains*

The vent area within the tephra cone comprises heavily fractured dome-like lava bodies, many of whose near-planar fracture surfaces are coated with dark-orange to

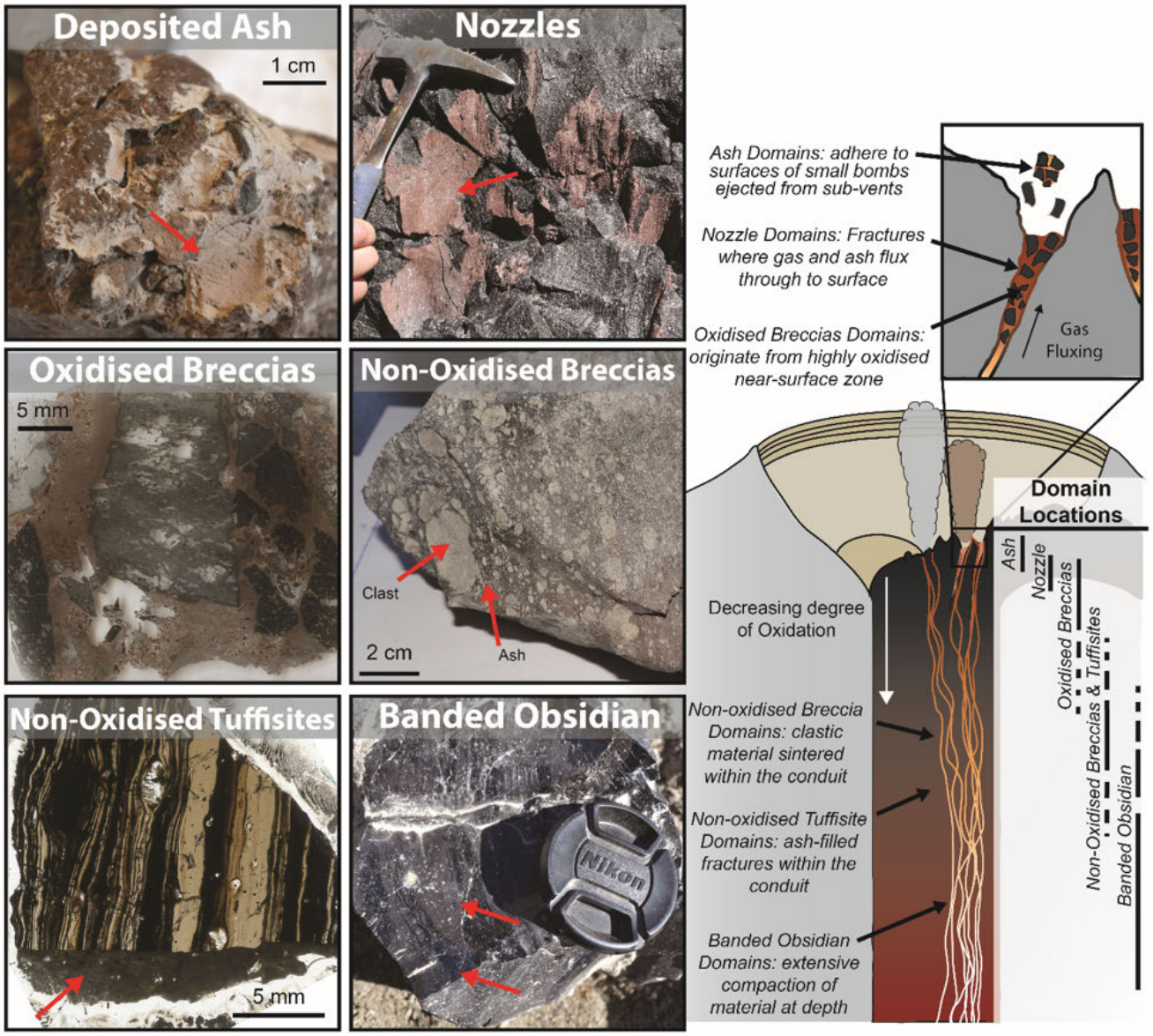

Figure 2: Schematic overview of the conduit and the relative depths of degassing that are preserved by different domains. Ash domains coat certain bombs and are adhered to surfaces upon ejection. Nozzles are sampled *in situ* at the surface of the flow within the vent complex. Oxidised domains originate in the near-surface zones whilst non-oxidised domains and banded obsidian are ejected from deeper in the conduit. Red arrows point to textures that characterise domain types.

red veneers (Figure 2). The veneers consist of heavily oxidised and sintered ash material adhered onto planar surfaces, and in certain locations the surface of the lava itself has been altered by oxidation. The lava is variably vesiculated and moderately microcrystalline, with distinct microlite-rich bands. Fracture orientation is unrelated to the orientations of the bands or vesicles. Microlites are <50 µm in length and are predominantly plagioclase and pyroxene; some devitrification textures are locally present [see also Magnall et al. 2018]. Sub-rounded bubbles are also present (see banded obsidian description).

4.1.3 *Breccias and Tuffisites*

Bomb textures at Cordón Caulle are complex (e.g. Figure 2). Many bombs from this eruption are breccias, with domains of pumice and angular obsidian separated, but sintered together, by fine-grained (µm- to mm-sized), variably oxidised ash matrices. Breccias form in the conduit and are then explosively expelled as bombs. Breccias and tuffisites are subdivided into two groups based on the intensity of their oxidation. Oxidised domains display heavy oxidation of clasts or matrix ash, expressed as deep orange to red colours, whilst non-oxidised domains show little or no oxidation of

components, and vary from white-grey to light pink-orange in colour. The oxygen fugacity of the environment, and degree of oxidation of samples, will change towards the surface due to increased interaction with oxidising, atmospheric gases or loss of reducing agents (e.g. hydrogen) [Furukawa et al. 2010; Moriizumi et al. 2009]. Thus more oxidised domains are thought to represent degassing closer to the surface, with greater interaction with the atmosphere than their less-oxidised counterparts.

4.1.4 *Oxidised Breccia Domains*

Oxidised breccias sampled from the vent are defined by their heavily oxidised (orange to red in colour) interstitial ash matrices (Figure 2). Centimetre-sized clasts within the breccia domains comprise dense or banded obsidian, with some bubble bands present. Some clasts have densely micro-cracked cores and others contain cristobalite within vesicles. Vesiculated clasts have contorted bubble shapes and evidence of coalescence and fracturing of bubble wall films. Microlite populations in dense clasts are similar to those in nozzle samples. Oxidation affects the outer ~30–200 µm of clast surfaces and bubble walls. Interstitial ash matrices can either be microlite-rich and texturally similar to neighbouring clasts, implying a local source, or glassy and microlite-poor. The matrix material can exhibit alternating laminations of both fine-grained (~10–30 µm) sub-rounded shards and coarse-grained (<400 µm) angular shards, similar to tuffisites at this and other volcanic centres [Paisley et al. 2019; Saubin et al. 2016; Stasiuk et al. 1996; Tuffen and Dingwell 2005]. Ash matrix shard shapes vary from highly rounded to angular, depending on their size and degree of sintering.

4.1.5 *Non-Oxidised Breccia and Tuffisite Domains*

Many breccias and tuffisite veins within Cordón Caulle bombs have little or no oxidation of their hosts, clasts, and any interstitial ash or tuffisite material. Vesicle sizes increase towards the centres of larger (>0.5 m) bombs, suggesting post-fragmentation inflation. Centimetre- to decimetre-sized clasts are mostly pumiceous, with rare dense obsidian clasts. Individual pumiceous clasts also display spatially heterogeneous bubble sizes, with the largest, cm-sized bubbles in the clast interiors again indicating post-fragmentation vesiculation [Wright et al. 2007]. Clast edges are either rounded or straight, indicating a variable degree of post-fragmentation viscous deformation. Fine-grained (~30 µm), well-sorted, sub-rounded glassy ash constitutes the interstitial matrix and sinters the larger clasts together. Ash matrices are largely devoid of crystals or crystal fragments. Clast foaming and expansion can compact the surrounding matrix material.

Tuffisite veins are preserved in some pumiceous and dense obsidian bombs; they commonly have sub-parallel edges (Figure 2); and are <3 cm wide. Tuffisite ash is white to light pink-orange in colour, and is glassy with rare microlites. Individual ash shards in veins are rounded to sub-rounded in shape with sizes varying from 10–50 µm. The degree of sintering varies extensively both between and within tuffisite veins. Laminations within a single vein can display sintering textures spanning from necking and preservation of primary void space (common in coarse-grained >30 µm-sized ash laminations), to complete compaction and densification of ash (common in fine-grained <30 µm-sized ash laminations). However, there is not always a clear correlation between ash grain size and degree of sintering. Sintering of neighbouring shards can obscure their original shapes, particularly in strongly-compacted tuffisites, where only the presence of sub-micron-sized crystals delineate the shapes of individual shards [Tuffen and Dingwell 2005]. Vesiculation of shard cores has been observed within tuffisite material, with dense poorly-vesiculated rinds outlining their shapes (as described in Saubin et al. [2016]). Individual shards can show evidence for strain localisation and bubble coalescence akin to textures in pumice erupted during earlier stages of activity [Schipper et al. 2013]. Crystals are rare in tuffisites but when found are within larger clasts with surrounding glass or as broken crystal fragments. Paisley et al. [2019] describe one bomb type, which is largely excluded from this study–metre-scale, homogenous, grey and pumiceous bombs with rare pink-coloured tuffisite veins and dense obsidian clasts. These are not the focus of this study because they likely represent gas-driven flow of bubbly magma but are integrated into the discussion with reference to Paisley et al. [2019].

4.1.6 *Banded Obsidian Domains*

Dense banded obsidian is prevalent throughout the suite of bombs at Cordón Caulle. Large metre-scale bombs of banded obsidian are found on the distal ridge noted in Figure 1. Many bombs have adhering tuffisite ash on their surfaces (Figure 2), and contain cm-sized clasts of pumice or oxidised lithics. Domains of obsidian occur within breccia bombs as large cm-sized clasts or as mm- to cm-sized angular shards within tuffisite veins. Edges of banded obsidian domains are often sharp (Figure 2) unless influenced by post-fragmentation vesiculation, e.g. bomb inflation. Banded domains may contain vesiculated bands, with rounded mm- to cm-sized vesicles showing evidence for coalescence. Rare enclaves (50 µm to ~1 cm in size) of vesiculated, microlite-rich, dark-brown glass are noted in banded obsidian bombs and banded obsidian clasts within breccias. Enclaves can be fractured and all have been observed to have uneven boundaries. Phenocrysts are rare, and light-coloured glassy bands are largely devoid of crystals whilst darker bands have higher proportions of oxides and pyroxenes <1 µm in

size, or 'nanolites' as coined by Mujin et al. [2017]. Needle-shaped microlites of plagioclase and pyroxene are <50 µm in length, if present. Flow bands are deflected around large crystals, dense and lithic clasts. Banding is also seen within the lava, with breakout textures extensively described by Schipper et al. [2015] and Magnall et al. [2018]. Vesicles and voids in the flow are cristobalite-coated, with vesicle collapse preserved by parallel bands of cristobalite [Schipper et al. 2015]. Banded obsidian textures have previously been interpreted as zones of thoroughly compacted, formerly clastic material that had an initially high permeability prior to sintering and compaction [Tuffen and Dingwell 2005].

4.2 Chemical Analyses

4.2.1 *Sample Variation: Majors & trace elements systematics during eruption*

Average major and trace element concentrations for each sample and their associated errors are summarised in the Supplementary Material, with highlights discussed below. Matrix glass concentrations for the 2011-2012 eruptive materials average 71.8 ± 0.6 wt.% SiO_2, 14.2 ± 0.2 wt.% Al_2O_3 and 5.0 ± 0.2 wt.% Na_2O. *Bomb*, *vent* and *flow* samples have similar concentrations for each element (Supplementary Material 1), which correspond closely to those reported by Castro et al. [2013]. No systematic variations in major elements are apparent when the *bomb* and *vent* samples are compared to the early Plinian phase and the concurrent *flow* phase [Castro et al. 2013; Schipper et al. 2019, this study]. Vent sample number V2 has higher SiO_2 and lower concentrations of compatible elements (e.g. CaO, MgO, TiO_2) than other samples, and is more microlite-rich resulting in a more evolved interstitial glass chemistry. Although individual samples plot within error of each other, positive correlations between certain major elements (e.g. FeO^t vs. TiO_2 or CaO vs. TiO_2) are apparent, and minor variation in microlite/phenocryst content would account for these trends (Figure S1). There is no correlation between Cl and K_2O (Figure S1), with K_2O values averaging 3.0 ± 0.2 wt.% but Cl varying between ~600 and 1900 ppm. Median Cl concentrations for the suite of samples analysed is ~1500 ppm, compared to ~1700–2100 ppm in plagioclase and clinopyroxene-hosted melt inclusions [Castro et al. 2013; Jay et al. 2014]. *Bomb* sample Cl concentrations range from ~1350 to ~1870 ppm. *Vent* samples V1 and V2 have lower than average Cl of ~1200 ppm and ~630 ppm (~70 % RSD) respectively. S concentrations are close to the detection limit at 10–20 ppm.

To compare trace element variation between samples, elements have been grouped based on their properties and behaviours in silicic systems. Group 1 elements (Sc, Ti, V, Cr, Mn, Co, Ni and Sr) are primarily compatible in the plagioclase, clinopyroxene and orthopyroxene-dominated phenocryst assemblage. Group 2 elements (Ba, Ga, La, Ce, Nd, Sm, Eu, Dy, Er, Yb, Lu, Y, Zr, Nb, Hf, Th and U) are the high field strength elements (HFSEs), rare earth elements (REEs) and other incompatible elements. Group 3 elements (Li, Rb, Cs, As, Sb, Mo, W, Cu, Zn, Ag, Cd, In, Sn, Pb, Tl and Bi) are elements known to be volatile, and they partition into magmatic and hydrothermal fluids and vapours. Group 3 can be further subdivided into 3 sub-categories; alkalis (Li, Rb and Cs), predominantly OH-complexing elements (As, Sb, Mo, W) and predominantly S- and/or Cl-complexing elements (Cu, Zn, Ag, Cd, In, Sn, Pb, Tl and Bi) [e.g. Churakov et al. 2000; Pokrovski et al. 2013; Wahrenberger 2002; Webster 1990; Zajacz et al. 2008]. *Bomb*, *vent* and *flow* samples cluster around a mean concentration for each trace element (Supplementary Material 1), plot within error of each other, and are comparable to bulk and glass analyses from the 1922, 1960 and 2011–2012 eruptions [Castro et al. 2013; Daga et al. 2014; Gerlach et al. 1988; Jicha et al. 2007].

There are no systematic differences between the different components of the hybrid phase of activity (*bomb* vs. *vent* vs. *flow*) in Group 1, Group 2 and most Group 3 elements (Figure S1). Subtle positive correlations between elements in Group 1 (e.g. Zr vs. Th) and in Group 2 (e.g. Co vs. Mn) are significant at the 95% confidence interval (Figure S1), although samples remain within error of each other. At the sample scale, Group 3 elements do not show the same systematic, strong correlations (at a 95% confidence interval) with either Group 1 (compatible) or Group 2 (incompatible) elements. Certain elements (Cr, Ni, Cu, Cd, In, Tl and Bi) have large % RSDs (>24 %) due to variability across the sample suite (Supplementary Material 1). *Vent* and *flow* samples have greater % RSDs in all elements than *bomb* samples. Tl, Bi and In concentrations are subtly different in the three sample categories (Figure 3A–B), with *vent* samples having the lowest median concentrations. Median *bomb* and *flow* sample concentrations cluster at ~14 ppm Cu, ~0.45–0.65 ppm Tl, ~0.1–0.15 ppm In and ~0.07 ppm Bi. *Vent* samples cluster at ~10 ppm and 22 ppm Cu but have lower Tl (0.15–0.4 ppm) and In (0.06–0.1 ppm) concentrations. Vent samples cluster around ~0.04 ppm Bi except for V2 (~0.12 ppm Bi). These groupings, and the large spread of concentrations, become more apparent when individual analyses are plotted (Figure 3C–D).

4.2.2 *Domain Variation: Trace element and Cl systematics from depth to surface*

Although few systematic variations in composition are observed between samples on a macroscopic scale, there is a large spread in the concentrations of certain elements within samples (as evident from the high % RSDs). Textural domains within individual samples (Subsection 4.1) can be chemically distinct from each

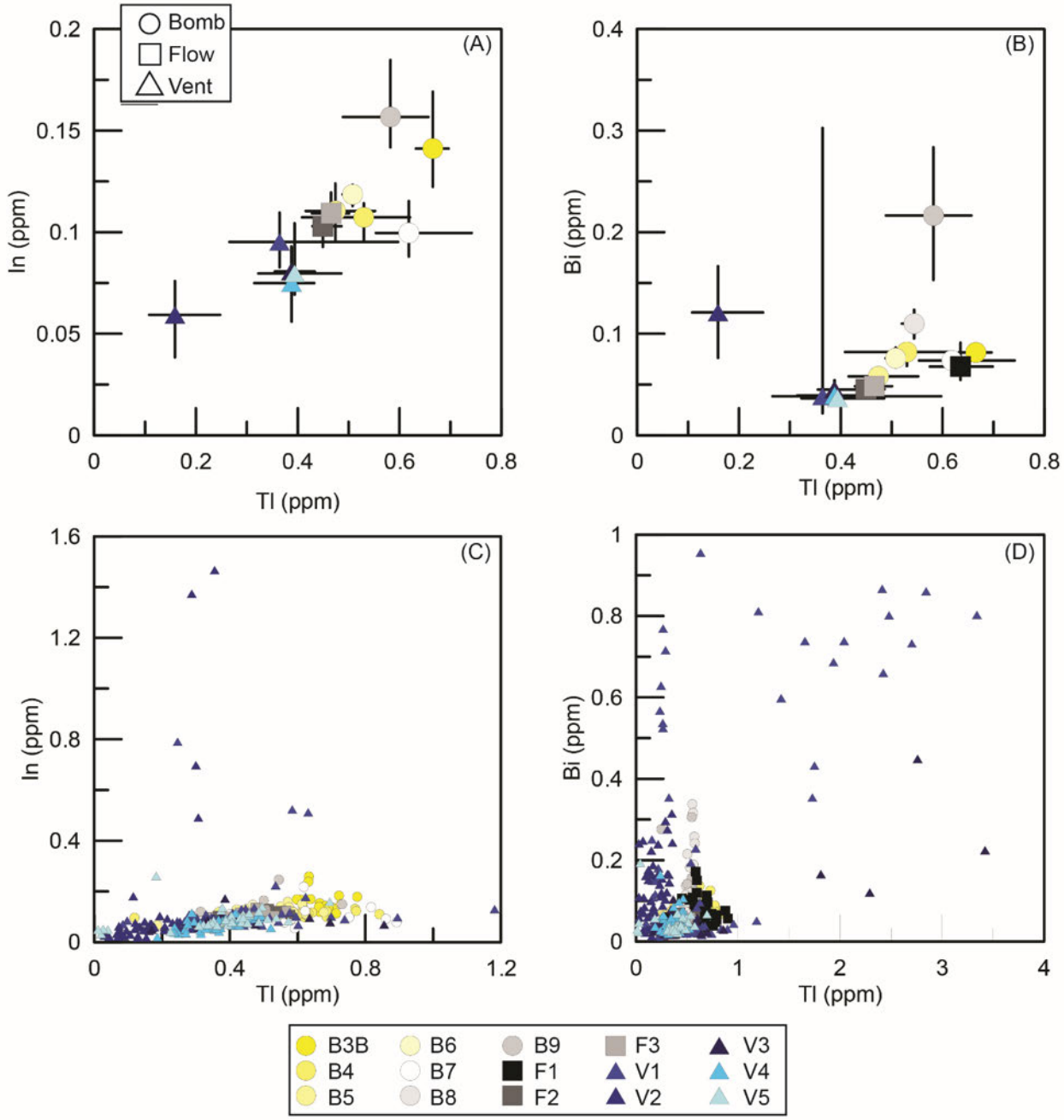

Figure 3: Comparison of median Tl, In and Bi concentrations of *bomb* (circles), *flow* (squares) and *vent* (triangles) samples from the 2011–2012 eruption ([A] and [B]). Error bars extend to the 25th (minimum) and 75th (maximum) percentiles. All three elements are known to be highly volatile. *Vent* samples, which were erupted towards the end of the eruption, have lower median concentrations of In, Tl and Bi than *bomb* and *flow* samples, which were erupted early in the eruption during the low-intensity explosive phase and during hybrid activity. This suggests a progressive loss of volatiles from the system with eruption duration. [C] and [D] show individual analyses from *bomb*, *flow* and *vent* samples and highlights the wide variance of concentrations within individual samples, particularly those from the vent. [C] Tl and In concentrations decrease linearly from early *bomb* samples to late *vent* samples. [D] *Vent* samples cluster at lower Tl and Bi concentrations than *bomb* or *flow* samples. Anomalously high volatile Tl, Bi and In concentrations in domains within V1 and V2 record complex processes that overprint the progressive degassing signature (see Section 5).

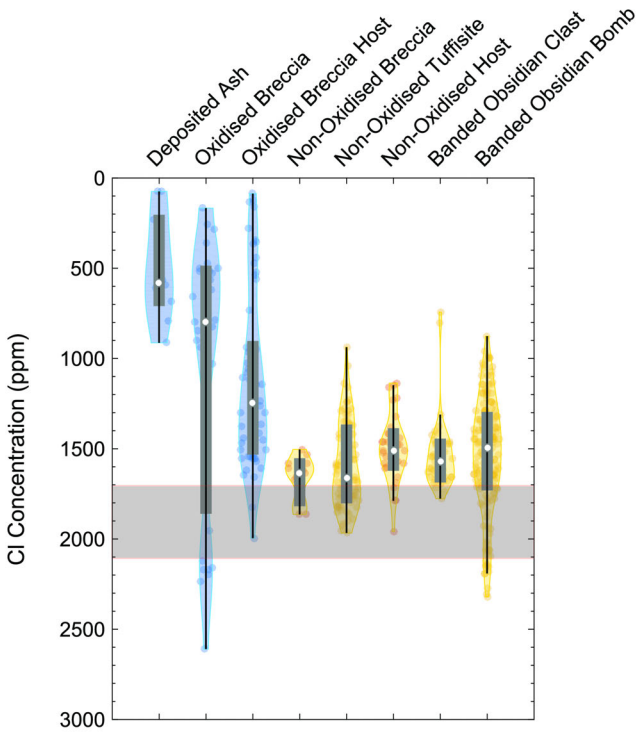

Figure 4: Violin plot highlighting median Cl concentrations for each textural domain (white circles) with their associated interquartile ranges (grey boxes), total ranges (black lines) and distribution of individual analyses (shaded areas and circles) (Bechtold, 2016). Domains are from *vent* (blue) and *bomb* (yellow) samples. Shaded box represents range of Cl concentrations in melt inclusions [Castro et al. 2013; Jay et al. 2014].

other, with significant variations in element concentrations observed at the interfaces between domains or across textural features.

Domain Chemistry Comparison

Chlorine concentrations and distributions vary for each domain (Figure 4). Deposited ash domains have a median concentration of ~640 ppm. Oxidised breccia material has a similar median Cl concentration but a significantly larger spread with a range of ~200–2000 ppm (Figure 4). Oxidised breccia host material has a median concentration of ~1250 ppm but areas can have <500 ppm Cl. Non-oxidised domains have narrower distributions and higher median Cl concentrations than the oxidised domains. Breccias (~1630 ppm) and tuffisites (~1670 ppm) have slightly higher Cl concentrations than their host material (~1510 ppm). Banded obsidian bombs and clasts have median concentration of ~1500 and ~1570 ppm respectively. Certain bands within banded obsidian bombs have Cl concentrations comparable to those recorded in melt inclusions from this eruption (Figure 4). No nozzle domains were analysed for Cl. Other elements (e.g. SiO_2, Al_2O_3, TiO_2 and CaO) do not vary extensively with textural type. Ash domains have lower median concentrations of MnO, MgO, FeO^t and K_2O, and a higher median Na_2O concentration than other domains. Domains in *vent* samples have wider total ranges than other domains.

The domain-host ratio defines the ratio of elemental concentrations of a domain, such as a tuffisite or ash matrix, with their respective host, e.g. $Li_{Tuffisite}/Li_{Host}$. Elemental enrichment or depletion relates to sources or processes (see Section 5). Figure 5 summarises the domain-host ratios for many elements from Groups 1, 2 and 3 whilst Table 1 denotes the elements that have a domain-host ratios outside of error of unity. We see no systematic enrichment or depletion in Group 1 or 2 elements within textural domains when compared to their hosts, with the exception of V that is enriched in oxidised domains and variable in non-oxidised domains. Group 3 elements show a wider range of variability, particularly within oxidised and ash domains. Alkali elements (Li, Rb, and Cs) are largely depleted in all domains. The predominantly OH-complexing elements (e.g. As, Sb, Mo) show little variation between domains with the exception of Sb that is very slightly depleted. Copper, Zn, Tl, Pb and Bi show the greatest amount of variation. Average Cu concentrations for all domains are within error of one (except V3 ash) but profiles across V1 breccia domain 1 and host highlight how Cu is systematically elevated, but highly variable, in the breccia ash (Figure 6). Zinc, Pb and Tl show depletions in several domains (Figure 5, Table 1). Bismuth is enriched in most domains (ratios between 1 and 3 in non-oxidised domains and ~6 to 16 in deposited ash domains) and Tl is enriched in the deposited ash domains (ratios between ~4 and 7).

Chemical Heterogeneity within Domains

In addition to the element variation observed between different domains and hosts, variation on the micron-scale occurs within many textural domains that we relate to diffusion in Subsection 5.3 (Table 2, Figure 7). Table 3 summarises elements showing systematic variations towards domain interfaces and the approximate length scales over which they vary. Figures 8, 9, 10 and 11 show how select elements vary towards or across interfaces in nozzle (Figure 8), oxidised (Figure 9), non-oxidised (Figure 10), and banded obsidian (Figure 11) domains. No analyses could be conducted to assess elemental variability across individual ash shards in ash domains due to their micron size. To summarise, in nozzle domains Cu, Tl and Pb show the most systematic variation (Figure 8), decreasing towards fracture surfaces over a ~500 µm-wide zone. In oxidised domains, Li, Rb and Tl decrease towards a clast interface in V2 which has a dense ~200 µm-wide, chemically distinct rim zone that has overprinted part of these systematic depletions (Table 3,

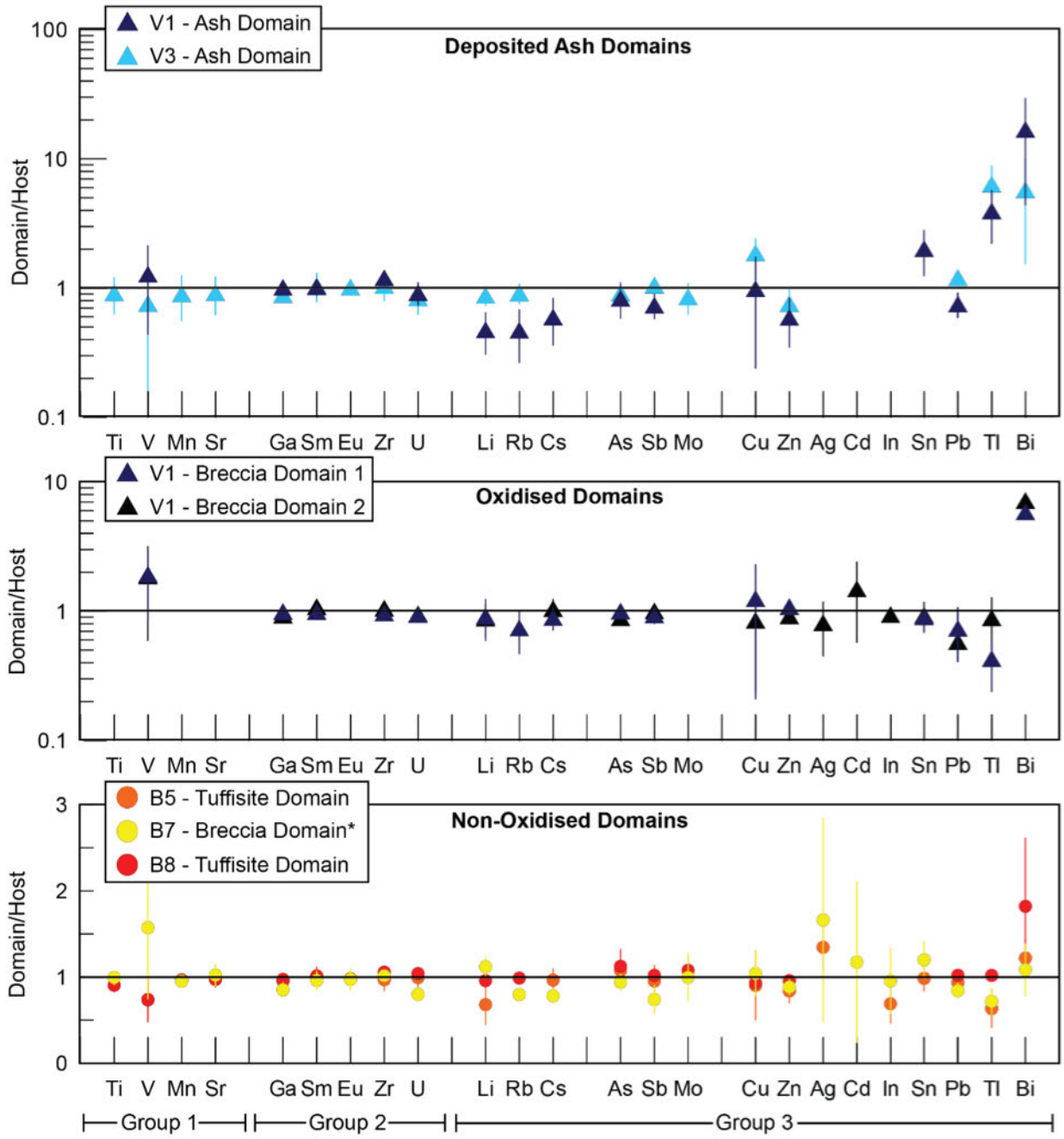

Figure 5: Domain-host ratios for select elements. Average concentrations for textural domains are normalised to their respective average host concentrations. Errors are 1 standard deviation. Domains are from *vent* (triangles) and *bomb* (circles) samples. Note use of log scale for ash and oxidised domains to account for high Bi ratios. Missing symbols indicate that the element was not analysed for in that domain.

Figure 9). Fewer profiles are observed in non-oxidised and banded obsidian domains with many examples showing no variation. Alkali elements (Li, Rb ± Na) are shown to decrease towards a clast interface (Figure 10) in a non-oxidised breccia and across bands in obsidian domains (Figure 11). Figures S3–6 compare elements discussed above (e.g. Table 3) to others discussed in Subsection 4.2.2 that do not vary towards interfaces, for data see Supplementary Material 2. Certain microlite-rich bands, likely induced by local degassing, have elevated TiO_2 and depleted Cl concentrations (e.g. Figure S2).

5 Discussion

5.1 Degassing: from eruption onset to decline

Previous geochemical studies of the 2011–2012 Cordón Caulle eruptive products have largely focused on the

Table 1 – Summary of elements that have domain-host ratios outside of unity. Elements are either enriched (En.) or depleted (Dep.) in domains. Group three is subdivided into alkalis, OH-complexing metals (OH^-) and S & Cl complexing metals (S, Cl). Alkali elements (Li, Rb, Cs) and certain Cl and S complexing elements (Zn, Pb, Tl, Bi) show the most variability. Element depletions in domains are common, although enrichment can be preserved (e.g. Bi). Group two elements show no systematic enrichments or depletions.

Domain type	Sample ID	Domain description	Group 1		Group 3						Sample comment
					Alkalis		OH^-		S, Cl		
			En.	Dep.	En.	Dep.	En.	Dep.	En.	Dep.	
Deposited ash	V1	Heavily oxidised				Li Rb Cs		Sb	Tl Bi	Zn Sn Pb	No Ag, Cd, In data available
Deposited ash	V3	Moderately oxidised				Li Rb Cs			Cu Pb Tl Bi	Zn	
Oxidised	V1 Domain 1	Breccia ash	V			Rb			Bi	Pb Tl	Variable Tl concentrations
Oxidised	V1 Domain 2	Breccia ash	V			Rb			Bi	Pb	
Non-oxidised	B5	Tuffisite		V		Li			Bi	Zn Pb Tl	Ash compared to a dense obsidian clast in breccia
Non-oxidised	B7	Breccia ash	V		Li			Sb		Zn Sn Pb Tl	
Non-oxidised	B8	Tuffisite		V					Bi	Zn	
Element comments			Cs is less variable than both Li and Rb						Cu highly variable within domains		

pumices from the initial Plinian phase, and tephra and ash from the subsequent 10 days of activity [e.g. Alloway et al. 2015; Castro et al. 2013; Collini et al. 2013; Daga et al. 2014]. The tightly constrained magma composition of this and the previous two eruptions (1922, 1960), along with interferometric synthetic aperture radar (InSAR) studies suggest a single, long-lived interconnected magma plumbing system has fed the past three eruptions [Delgado et al. 2016; Jay et al. 2014]. Alloway et al. [2015] argue that three co-genetic pockets of magma (defined by differing CaO and Sr concentrations), each undergoing varying degrees of plagioclase fractionation at different pressures, were tapped simultaneously during the paroxysmal phase of the 2011–2012 eruption. We find no chemical evidence to suggest a melt source different to the long-lived, pre-existing reservoir was tapped, or that the melt source evolved significantly, as this eruption progressed. Minor trends in major and trace elements (Figure S1) likely result from phenocryst and microlite growth. The compositional differences between samples, which may reflect differing degrees of crystallisation, are typically smaller than the chemical variance within samples. This indicates that most crystal growth occurred in the conduit, likely in the form of microlites that were not subsequently segregated, inducing small-scale, intra-sample glass heterogeneities much larger than inter-sample heterogeneity induced by differentiation.

Previous studies have been unable to constrain the volatile evolution of this eruption as the final erupted products have no systematic water variations and are degassed to near-atmospheric conditions, corresponding to the top tens of metres of the conduit (<0.35 wt.% H_2O, [Castro et al. 2014; Schipper et al. 2013]). Our trace element data show certain volatile elements (In, Tl and Bi) are much lower in concentration in *vent* samples than in the earlier *bombs*, erupted predominantly in June 2011, and the *flow* deposits, erupted during 2011 and 2012 (Figure 3). As *vent* samples represent the final, waning phase of activity in 2012, the hybrid activity arguably did progressively degas certain volatiles from the system during the course of the eruption.

A caveat of this study is sampling bias and eruption dynamics prevent the study of certain components of the eruption. *Vent* samples representing the early hybrid phase were not attainable due to their location in inaccessible parts of the lava flow and/or their burial. The analysed *vent* samples have been collected *in situ* (or nearby in case of erupted breccias) and represent vent processes, but only those at the end of the eruption. *Bomb* samples far from the vent site are thought to derive from earlier in the eruption sequence (Subsection 3.1) and smaller *bombs* from the vent are thought to represent the later, less energetic phases of the eruption. This means that our sampling of the eruption sequence is early and deep (*bombs*), followed by later

and surficial (*vent* samples). When comparing the elemental variation in different samples (discussed in the following sections) it is hard to definitively distinguish whether the concentration variations in mobile elements reflect changing gas compositions and ligand availability with time during eruption or depth, or the timescales of individual events (as short events will not be preserved by slow diffusing elements, Subsection 3.1).

5.2 Degassing: from depth to the surface

Textural domains within samples record numerous processes during magma ascent in the conduit, and chemical heterogeneity can be attributed to specific degassing events that occurred at different times and depths. Interfaces between such domains preserve information about their relative timing and are discussed in the next section. Many bombs have undergone post-fragmentation vesiculation, as demonstrated by breadcrust textures and increasing vesicle sizes towards bomb centres, but we instead focus on pre-ejection degassing processes. We estimate the relative conduit extraction depths of different bomb types and domains using knowledge of the eruption evolution, bomb textures and variations in Cl concentrations.

Surface uplift related to shallow laccolith emplacement (inferred to be ~20–200 m below the surface and <200 m thick) began on June 8th alongside vent constriction, Vulcanian blasting and low-intensity plume behaviour [Castro et al. 2016; Pistolesi et al. 2015]. The laccolith would therefore have been present, or at least developing, during ejection of all of the studied bombs. Although Vulcanian events can, in some cases, evacuate the top ~2 km of silicic conduits [e.g. Wright et al. 2007] the low H_2O in Cordón Caulle bombs indicate ejection from tens of metres depth [Schipper et al. 2013]–most likely above the laccolith intrusion or close to its roof.

It is not possible to accurately quantify the depths samples represent, due to the low preserved H_2O contents. Instead, we determine the samples represent processes in the shallow conduit (10s of metres to <200 m), the near-surface (top few metres of the conduit) or the surface environment. We use oxidation colouration, brittle-ductile textural features and Cl concentrations of different domains to compare their relative extraction depths. A heavily oxidised sample, for example, is more likely to have come from a shallower environment than a non-oxidised sample. Similarly, material that has undergone several generations of fractures followed by extensive viscous deformation, prior to bomb expansion, will have likely had a more prolonged in-conduit residence than material preserving only a single generation of brittle fractures [Tuffen and Dingwell 2005]. Thus it is assumed material with extensive viscous textures will have originated from deeper in the conduit than samples preserving predominantly brittle textures. Chlorine is largely retained in the melt until magma ascends into the near-surface, or is extruded as a flow or a dome, where a degree of open-system degassing occurs and Cl can be readily degassed into an available vapour phase as HCl [Edmonds et al. 2002; Lowenstern et al. 2012; Schipper et al. 2019; Villemant et al. 2008]. The loss of Cl in domains, such as heavily-oxidised and ash domains, constrains them and their processes to the near-surface environment whilst it is inferred that Cl-rich samples, such as banded obsidian domains, would have quenched at higher pressures, see below.

The lack of systematic chemical variation in elements predominantly controlled by fractional crystallisation (e.g. compatible and incompatible elements, Groups 1 and 2) allow us to isolate and focus on chemical heterogeneity induced by degassing (Group 3 elements) in different textural domains. Domains are discussed in order from deep to surface domains. Also general elemental variability, as represented by the size of the error bars in Figure 5, is high in the fine-grained ash domains within breccias and veins. This reflects the analytical detection limits and varied provenance of the ash particles, which derive from both the local host and deeper in the conduit (see below). We cannot definitively state whether heterogeneity in elements such as Cd, In and Ag relate solely to degassing processes or are a function of their concentrations being close to their limits of detection and thus these elements are not discussed in the following sections.

5.2.1 *Banded Obsidian Domains*

Banded obsidian bombs and clast domains represent relatively deeper fracturing in the system as supported by the high Cl concentrations in certain bands of microlite-free glass [Schipper et al. 2019]. The highest Cl concentrations, <2300 ppm (Figure 4), are comparable to the Cl concentrations (~1700-2100 ppm) found in melt inclusions in plagioclase and pyroxene crystals [Castro et al. 2013; Jay et al. 2014]. The extensive folding of thoroughly-sintered bands, removal of ash textures, and alignment of nanolites is consistent with a prolonged post-fracturing period of viscous melt relaxation.

Degassing in banded obsidian domains is largely recorded texturally as the majority of these domains have minimal chemical heterogeneity preserved. Textural evidence of degassing includes degassing-induced microlite crystallisation in concentrated bands and collapsed foam textures that record vesiculation and deflation [Gonnermann and Manga 2005; Tuffen and Dingwell 2005; von Aulock et al. 2017]. Vesicular, microlite-free bands within banded obsidian clasts were likely less degassed than microlite-rich, vesicle-free bands, allowing preferential bubble nucleation upon ejection.

It is impossible to confirm whether bands were chemically similar prior to juxtaposition or the bands have chemically homogenised. However, given some vari-

ation is recorded (e.g. Figure 11) it is likely chemical homogenisation has played a role. The exsolution or presence of a volatile phase (composed of major volatiles such as H_2O) is necessary for the formation of trace volatile depletions. Metal species diffuse towards the melt-gas interface and then partition into the volatile phase [e.g. MacKenzie and Canil 2008]. Chemical variation is largely lost because of the extended time the melt spends in high temperature conditions (above T_g) after a phase of gas mobility within a permeable fracture pathway. If high permeability is briefly sustained only the fastest diffusing elements (e.g. Li, Table 2) would significantly diffuse through the melt and partition into the gas phase during this timeframe. The subsequent residence of the system at high temperature would be sufficient to facilitate diffusive re-equilibration and remove any initial compositional variation, assuming there is no rapid quenching. Evidence for a protracted period of high-temperature, post-fracturing melt relaxation includes complete removal of initial porosity and extensive ductile deformation of bands. When compositional heterogeneity is chemically preserved (Subsection 5.3) the timescale recorded represents every process from initial fracturing and juxtaposition of the two contrasting bands, through their healing, bomb ejection and cooling, as only the last process will quench the glasses and lock in any chemical variation. Geochemical signatures of degassing include the large range in Cl concentrations within banded obsidian bombs. Low Cl concentrations are restricted to bands that have undergone degassing-induced microlite crystallisation of oxides, bands also have elevated TiO_2 and MgO (Figure S2). Rare depletions of Li (and Rb) in dense bands in banded obsidians (Figure 11) indicate that heterogeneity of rapidly-diffusing trace volatiles can be preserved by quenching. However, there are no clear depletions of slower-diffusing species (e.g. Cs, Tl, Pb, see Table 2) within the same bands, reflecting diffusion-limited degassing [e.g. Gardner et al. 2012; MacKenzie and Canil 2008], where there is insufficient time for metals to diffuse to a gas-melt boundary. Textures and chemistry therefore point towards gas loss from these bands, presumably when they were highly permeable channels prior to their healing.

Banded obsidian clasts within breccias have a more restricted range of Cl concentrations than bombs entirely composed of banded obsidian (Figure 4). Our interpretation is that fracturing and entrainment of the obsidian clasts within breccias was constrained to the top ~200 m of the conduit, above the laccolith, but occurred at greater depths than the shallow sub-vent structures (top few metres of the conduit) where flow emplacement began [Castro et al. 2016; Schipper et al. 2013]).

5.2.2 *Non-Oxidised Breccias and Tuffisites Domains*

Although breccia bombs and tuffisite-hosting bombs are texturally distinct, their origins are arguably similar. Breccias are formed when there is fracturing and fluxing of material on a scale of centimetres to metres within the conduit [e.g. Gonnermann and Manga 2003]. Tuffisite veins form when a fracture propagates through a dense melt-rich plug, with fluxing clastic material in the vein sintering together and eventually sealing the permeable fracture pathway [e.g. Castro et al. 2012; Saubin et al. 2016; Tuffen et al. 2003]. Both processes involve a fracturing event generating a permeable pathway for gases, before sealing by sintering and compaction processes. As such, we will not refer to them as two separate processes but rather the same process on two differing scales, as breccias can be considered the clastic fill of tuffisite veins that are larger than the dimensions of the ejected bombs. Their non-oxidised textures with many ductile features (Subsection *4.1.5*) and chemistry (intermediate Cl concentrations, Figure 4) suggest derivation from greater depths than the surface vent nozzles and thus breccias and tuffisite veins represent fracturing processes pervasive throughout the upper conduit at Cordón Caulle.

Textural and chemical evidence from these domains aid assessment of the roles of permeable zones as pathways for gas and ash fluxing. Schipper et al. [2013] use a vesiculation model to constrain the onset of permeability via connected bubbles in the ascending magma to a depth of 1–1.5 km. Our breccia clast textures (dense vs. highly vesicular, e.g. Figure 10) suggest extensive connectivity of permeable zones that enabled juxtaposition of melts of differing original volatile contents. Volatile-rich deeper melts rapidly vesiculate as H_2O solubility drops on approach to the surface, with clast expansion compacting the ash matrix of breccias (Figure 10). The lack of water variations in the residual glasses, however, prevent us from quantitatively constraining the transport distances of clasts within fractures [e.g. Saubin et al. 2016]. Tuffisite veins have previously been shown to be pathways for gas fluxing at Cordón Caulle [Paisley et al. 2019] and data presented in this study further highlight their role as pathways for gas transport. The matrices of breccias and tuffisites, areas that would have been most permeable to gases, are largely depleted in volatiles (e.g. Pb and Tl), where heterogeneity is preserved Figure 5), although Bi enrichment is a notable exception and discussed separately (Subsection *5.2.6*). Paisley et al. [2019] propose that vein depletions may result from metal scavenging from individual shards or tapping of more degassed melt prior to fracturing, and we argue that the former scenario is more likely. We use the characteristic diffusion length of elements (Table 2) to compare the time required for metals to diffuse across a distance equivalent to the shards' radii. Shards are ~30 µm in diameter and only minutes of fluxing would be required for Tl to

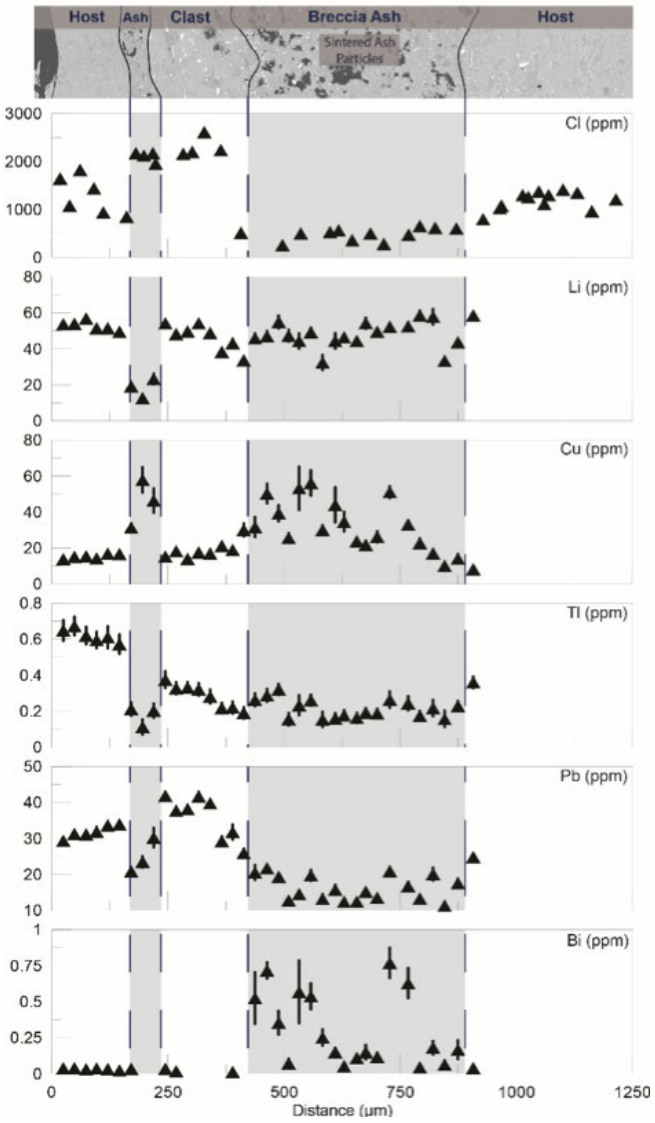

Figure 6: Trace element profiles across an oxidised breccia matrix between two clasts from a *vent* sample (V1 Domain 1). Matrix ash is largely depleted in volatiles (e.g. Cl, Pb and Tl) compared to its host, Bi and Cu are exceptions. Clasts entrained within the matrix can have distinct compositions to both the host and ash matrix. Bi is below detection limits within parts of the ash (~150–200 µm) and the entrained clast. Laser analyses did not extend into the host (>900 µm). Error bars are ±2 standard error, no error bar indicates error smaller than symbol size.

diffuse across shards and partition into the gas phase. Final species concentrations would reflect their partitioning behaviour under these eruptive conditions and species activities in the gas phase [Zajacz et al. 2008]. Further evidence of the active stripping of elements by a fluxing gas phase is the degassing-induced elemental gradients (in alkalis, Tl and Pb) observed at domain interfaces (Table 3, Subsection 5.3).

5.2.3 *Oxidised Breccias Domains*

Heavily oxidised domains with largely brittle textures represent fracturing and degassing processes in the sub-vents and top few metres of the conduit during ash jetting and small explosions, consistent with the lower median Cl concentrations of ash shards and clasts (Figure 4; Schipper et al. [2013] and Villemant et al. [2008]).

Clasts within these breccias are a combination of material from three sources: *deep*, *local* and the lava *flow* (Figure 2). Highly vesicular clasts, with contorted vesicles, within breccias are sourced from *depth* with their volatile-rich melt rapidly vesiculating at the surface. Sintered ash-filled vesicles that intersect bomb rims and clasts with partially oxidised, collapsed foam textures, indicate some vesiculation occurred prior to these clasts reaching the surface environment. *Locally*-sourced material includes clasts and ash shards within the matrix that have similar microlite textures to the nozzle material (the host walls of the sub-vent fractures). Cristobalite-bearing clasts in breccias are evidence of *lava flow* material being entrained within the nozzles as cristobalite has only been observed in the rhyolite flow at Cordón Caulle [Schipper et al. 2015]. Previous studies have shown how fractures are capable of transporting both local and deeper-derived material [Saubin et al. 2016]. The mixed provenance of clasts reflects how these fractures are the surface expressions of deeper permeable networks, with explosions excavating and incorporating shallow-derived material. Pressure build-up in the system, due to blocking of nozzles or overpressure at depth, led to the explosive expulsion of these heavily oxidised breccias.

There is strong chemical evidence of degassing in the near-surface. Pb and Tl are depleted in matrix material, more so than the matrix of non-oxidised domains (Figure 5). One entrained clast within the matrix (Sample V1, Figure 6), with its distinct Cl, Tl and Pb concentrations, is an example of the juxtaposition of variably degassed melt fragments. Figure 6 graphically shows why RSDs for *vent* samples are greater than their *bomb* counterparts (see Supplementary Material 1). Volatile element RSDs are higher in samples V1-V5 because they comprise of diverse, variably-degassed clast types and domains that have subtly different volatile concentrations, resulting in higher standard deviations. This is most clearly noted in Li, Cu, Rb, Cd, In, Cs, Tl, Pb and Bi where RSDs are >30 % higher than the respective RSDs in *bomb* samples. The RSDs for the remaining Group 1 and Group 2 elements are also higher in *vent* samples: 10–20 %, as opposed to <10 % in *bomb* samples, which reflects microlite growth. *Vent* and *flow* samples have undergone some microlite growth and devitrification. Laser ablation is a mini-bulk analysis of glass and microlites. When averaging multiple analyses, microlite growth will not affect the accuracy of the calculated mean, as no fractionation between crys-

tals and melt occurred, but it will affect precision as laser pits will have variable proportions of microlites. This is especially apparent at smaller spot sizes of <50 µm, which are comparable to microlite dimensions in these samples. If higher RSDs in volatiles were also due to microlite growth then Group 3 elements would be expected to show a similar increase in % RSD (from <10 to 10–20 %) but this is not the case. Furthermore, individual breccia clasts can be chemically distinct. Thus, we argue the high RSDs of volatile elements in *vent* samples, particularly oxidised breccias (V1–V2), represent the complex degassing histories of their constituent clasts up to and prior to entrainment in the sub-vent areas.

5.2.4 *Nozzle Domains*

Nozzles are the surficial, sub-vent structures, sampled *in situ*, which were seen to host regular explosions by Schipper et al. [2013] and are the sources of the oxidised breccias discussed above. Field and textural evidence for the channelling of gases through these features includes extensive oxidation and ash adhesion to the surfaces (Figure 2). Degassing of volatile elements into these features is preserved by elemental gradients of Cu, In, Tl and Pb, and their diffusion is discussed later. Elemental depletions towards surfaces imply that metals are diffusing towards the melt-gas interface and partitioning into the gas phase. This is strong evidence that fractures at Cordón Caulle can actively degas local melt, as shown for Chaitén [Berlo et al. 2013; Castro et al. 2012].

5.2.5 *Ash Domains*

Ash domains, only found on the surfaces of samples, form in the surface environment when ash fluxes from a high temperature, highly oxidising, and pressurised environment (nozzle) to a lower temperature and low-pressure environment (i.e. air) and adheres to the surfaces of ejecting bombs (Figure 2). As individual shards are only microns across and would quench almost instantly in the surface environment, they must adhere to bombs during their ejection through the sub-vent structures and not in the ash plume. We infer the adhesion of dark-red ash to surfaces (e.g. nozzles) occurs slightly deeper (where it is more oxidising) than light-pink ash adhesions as the latter are commonly adhered onto red oxidised surfaces but red oxidised ash is not observed adhered to light-pink ash. The lighter pink colour would also suggest oxidation of this ash occurred in a slightly more aerated, surface environment. Low chlorine concentrations (Figure 4) support the hypothesis that these domains originate in the surface environment where Cl can readily degas [Villemant et al. 2008]).

The chemical signatures in ash reflect degassing during its upward trajectory through fractures and at the surface. Low ash-host ratios in Li, Rb and Cs might be suspected to reflect alkali depletion in the ash (Figure 5). For example, V1 ash has absolute concentrations of ~30 ppm Li, ~30–70 ppm Rb and ~2–4 ppm Cs, which are slightly lower than the Cordón Caulle average. However, the host has ~43 ppm Li, ~76 ppm Rb (but <120 ppm in certain clasts) and ~5.5 ppm Cs, which are significantly higher than average concentrations, and so the apparent depletions largely reflects host enrichment. The low Cl concentrations of ash domains (Figure 4) indicates some degassing occurred in a shallow environment. In places Li and Cl variation correlate (e.g. V2 dense rim) and alkalis are known to complex with Cl [e.g. Pokrovski et al. 2013]; thus their mobility, and concentrations, could be tied to the loss of Cl from the small shards in the shallow regime.

Depletions in trace metals such as Zn, Sn and Pb within the ash likely represent scavenging of metals by fluxing gas at depth and as the ash shards are transported towards the surface. Zinc and Pb are slow diffusing elements, requiring hours to diffuse tens of microns in a melt with a low water concentration (Table 2). However diffusion, and thus scavenging and metal loss, would be orders of magnitude faster in melts with a higher residual water concentration [Mungall 2002], e.g. melts at depth and melt shards fluxing through tuffisite veins. Thallium is a highly volatile element, with its monovalent state allowing it to complex with Cl and S and form oxide or hydroxide species [Baker et al. 2009; Churakov et al. 2000]. Changing conditions (temperature and oxidation) will affect the stability of Tl complexes and total concentrations in the gas phase as it goes from a sub-surface vapour to a surface aerosol within the plume. Thallium shows significant enrichment in ash domains, but depletions in the matrix ash in breccias and tuffisites formed in the conduit where it has been rapidly scavenged (Subsection *4.1.5*, Table 1). Ash within plumes interacts with the concurrent gas phase [Bagnato et al. 2013; Delmelle et al. 2007; Moune et al. 2006] providing surfaces for adsorption or resorption of Tl, with only seconds required to diffuse through a <10 µm-sized shard. The comparable dimensions of ash shards and laser spot sizes would normally preclude the distinction between these two processes. However, Tl enrichment of the vesicle walls in direct contact with the sample exterior of an oxidised breccia bomb (Figure 9A) is evidence for Tl resorption in a small window of the surface regime. Thus, we argue that ash material has scavenged and resorbed Tl from the plume at the surface. Resorption would not be preserved in Zn and Pb, since their lower diffusivities and the rapid quenching of ash shards preclude diffusion across this short length scale. Zinc, Pb and Tl are known to complex with Cl in fluids and vapours [Churakov et al. 2000; Zajacz et al. 2008], and Cl favourably partitions into a vapour phase in the shallow environment [Villemant et al. 2008; Webster 1990]. Thus, the shallow degassing of Cl in the system could be aiding

Table 2 – Summary of diffusion coefficients (D, $m\,s^{-2}$) calculated using equations from Mungall [2002] at an eruptive temperature of 895 °C [Castro et al. 2013], assuming a water concentration of 0.25 wt.%, a reasonable estimation for the Cordon Caulle upper conduit [Castro et al. 2014; Schipper et al. 2013]. The characteristic length scale of diffusion equation, $x \sim \sqrt{Dt}$—where x is distance (m) and t is time (s)—is used to compare the time required for elements to diffuse over a known distance given the calculated D values. Order of diffusivity of elements used in Subsection 5.3: $D_{Na}>D_{Li}>D_{Tl}>D_{Rb}>D_{Pb}$.

Element	D ($m\,s^{-2}$)	Time for elements to diffuse		
		5 µm	15 µm	25 µm
Na	1.49×10^{-10}	0.2 s	2 s	0.1 min
Li	3.72×10^{-11}	1 s	6 s	0.3 min
Tl	2.21×10^{-12}	11 s	102 s	4.7 min
Rb	1.54×10^{-12}	16 s	147 s	6.8 min
Cs	6.07×10^{-14}	7 min	1 hr	3 hr
Pb	7.17×10^{-15}	58 min	9 hr	24 hr
Zn	1.13×10^{-15}	6 hr	55 hr	154 hr
Cu	1.06×10^{-15}	7 hr	59 hr	164 hr
Bi	5.55×10^{-17}	125 hr	1126 hr	3128 hr

the scavenging of certain metals.

In summary, we have strong textural and chemical evidence that magma fracturing and degassing is prevalent throughout the system at Cordón Caulle. Chemical ratios imply that the gas phase carrying ash shards through fractures actively strips these ash shards of their volatiles, with this process more readily preserved in the surface samples where volatiles are stripped from both shards and host material.

5.2.6 *Bismuth Behaviour at Cordón Caulle*

Bismuth was degassed and depleted as the eruption progressed. At Cordón Caulle any Bi enrichment is constrained to within permeable zones where volatiles actively fluxed (e.g. breccia matrices, tuffisite veins and ash domains, Figure 5). Paisley et al. [2019] also observed this signature and argued it is due to gas fluxing and adsorption of Bi. Given its low diffusivity, Bi would require considerable time to be resorbed into ash shards >30 µm across (Table 2), making it an unlikely method of enrichment, but adsorption onto surfaces could occur [Ruggieri et al. 2011]. Alternatively, the source material for the ash matrices could be Bi-enriched relative to the vein and breccia hosts. Bismuth is a highly volatile element, commonly associated with mafic magmas and found enriched in plumes [Guo and Audétat 2017; Mather et al. 2012]. Thus, Bi enrichment could be suggestive of the transfer and incorporation of volatiles from a mafic magma to the silicic magma at depth. Large errors for Bi domain-host ratios (Figure 5) are due to both local (Bi depleted) and distal (Bi enriched) glass being analysed. Cu and V show more variable behaviours than other elements, including enrichment in these ash and oxidised domains (Figures 5 and 6). Both are associated with mafic melts, although V is not volatile [Guo and Audétat 2017; Mather et al. 2012]. We argue that this enrichment is evidence for the potential interaction of a volatile-rich mafic melt with the silicic melt in the Cordón Caulle system either before or during the eruption. Rare vesiculated enclaves of more primitive melt preserved in banded obsidian domains (Subsection *4.1.6*) and vesiculated mafic enclaves observed within the lava flow by Ruprecht and Winslow [2017] are evidence for mafic interaction at depth.

5.3 Timescales of Degassing Events

Element gradients develop when two melts of differing concentrations are juxtaposed against each other, with elements diffusing from high to low concentrations as defined by Fick's law of diffusion [Fick 1855]. Trace element and H_2O profiles forming at the margins of tuffisite veins have been previously used to assess their diffusive lifespans [Berlo et al. 2013; Cabrera et al. 2011; Castro et al. 2014]. To constrain the timescales of processes related to element gradients in Figure *4.2.2* we fit diffusion models to multiple trace element profiles with solutions of the 1D diffusion equation:

$$\frac{\partial C}{\partial t} = D\,\frac{\partial^2 C}{\partial x^2} \qquad (1)$$

where C is the concentration of element X (ppm), t is time (s), x is position (m) and D is the diffusion coefficient of element X ($m^2\,s^{-1}$). Diffusion coefficients are a function of temperature (T) and composition [Zhang et al. 2010], which is assumed to be 895 °C for the 2011–2012 Cordón Caulle magma [Castro et al. 2013]. The order of the calculated diffusion coefficients is $D_{Na}>D_{Li}>D_{Tl}>D_{Rb}>D_{Pb}$ (Table 2; Mungall [2002]). Equation 1 was solved using an explicit finite-difference model for all profiles [Crank 1975]. For profiles towards fracture interfaces (Figures 8, 9 and 10), the model assumes element X is diffusing in a semi-infinite media (Figure 7A). The pre-fracture melt concentration is assumed to be equal to the median, far field concentration, $[X_i]$. The boundary concentration of element X, $[X_b]$, is assumed to be in equilibrium with the gas phase and constant throughout. Calculated diffusion profiles shown in Figure 11 are based on a different configuration (see Figure 7B). Two semi-infinite media are assumed to come in contact with each other and then diffusion commences. Accordingly, the initial boundary concentrations within each media are equal to their respective initial far field concentrations, $[X_j]$ and $[X_k]$. But, unlike profiles towards fractures, the boundary concentrations at the interface between the two media are not constant throughout. We assume no modification occurred to the profiles after quenching

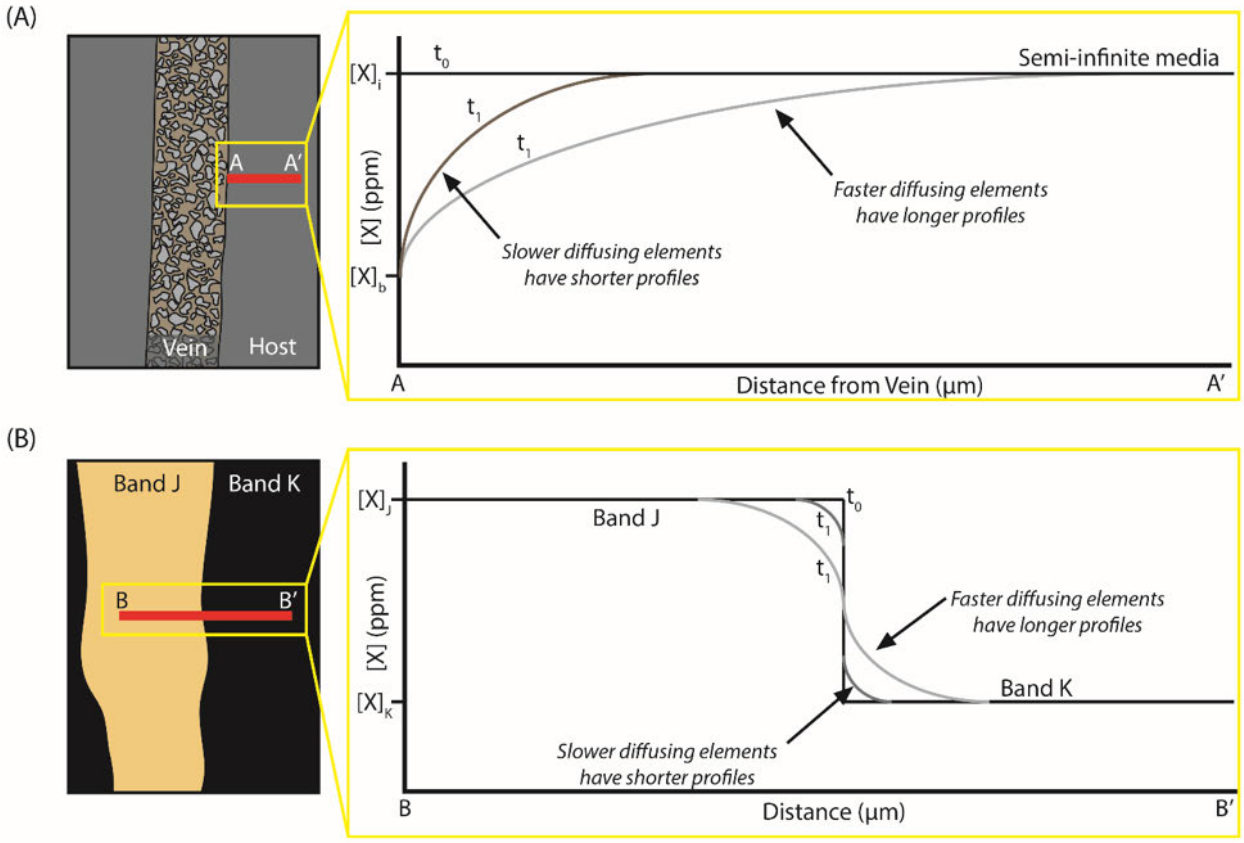

Figure 7: Conceptual model summarising the initial and boundary conditions of the explicit finite-difference model used to estimate timescales of degassing processes (t_1). Analyses via LA-ICP-MS or EPMA are represented by the red line. [A] A fracture or surface undergoes gas fluxing and is texturally preserved as a tuffisite vein or fracture surface. An initial concentration, $[X]_i$ at t_0, is assumed to equal the far-field value of the profile. The boundary concentration $[X]_b$ is assumed constant throughout degassing ($t_0 \longrightarrow t_1$). [B] Banded obsidian preserves old fractures. Two bands (J and K) are assumed to have different initial concentrations, $[X]_j$ and $[X]_k$, at t_0, which are equal to the far-field concentrations within the bands, away from the interface. Faster diffusing elements will have longer profiles. Timescales estimates (t_1) are order of magnitude estimates due to errors associated with analysis and calculation of trace element diffusion coefficients.

of the melts therefore the timings calculated represent one diffusing event that encompasses all processes from fracturing, degassing and sintering, through to bomb ejection and cooling/quenching. Given analytical uncertainties and the uncertainties of the calculated diffusion coefficients for these trace elements, the modelled timescales should be considered order of magnitude estimations for the timing of events. Diffusion profiles are most commonly found neighbouring fracture surfaces in breccia or nozzle samples. Although chemical variability is found in banded obsidian (see Figure 11; Figure S2), and is associated with each band being chemically distinct, only one clear chemical gradient was analysed, constraining the diffusion timescale between two bands. Only certain Group 3 elements were found to preserve diffusion gradients, these are Li, Na, Rb and Cs (the alkalis) and Cu, Tl and Pb. Chlorine, a ligand, was also found to form a short diffusion gradient in V2 (rim). Four examples are considered here, and summarised in Table 3 highlighting the timescales of different events within the conduit (from depth to the surface) that relate to specific textural domains.

First, calculated diffusion gradients on the order of seconds (Li) and minutes (Rb) observed between two neighbouring bands in a small banded obsidian bomb (Figure 11) suggest degassing, particle sintering and compaction occurred within these short timescales, in line with experimental studies [Gardner et al. 2018; Wadsworth et al. 2016]. These bands quenched very quickly after their juxtaposition, preventing the complete homogenisation of these mobile elements. Rb diffusion is calculated to be slower than that of Tl (Table 2) but Tl has no preserved variation across these bands. This suggests there was minimal initial difference in the concentration of Tl between the two bands.

Second, gradients of Li and Na observed at the edge of a banded obsidian glass shard, within a non-oxidised pumice breccia (Figure 10), suggests the interstitial ash (and clast edges) underwent only minutes of degassing after a fracturing event, prior to the expulsion

Table 3 – Summary of the length scales of element variability preserved at certain domain interfaces and the calculated timescales, in brackets, of the related ed degassing processes. Alkali element gradients are found in multiple domains whilst slower diffusing elements (e.g. Tl, Pb) only have preserved gradients in more surficial domains.

	Nozzle domains		Oxidised domains		Non-oxidised domain	Banded obsidian domain
Samples	V4, V5	V1	V2		B7	B12
Interface description	Planar fracture surface	Bubble-glass	Ash-dense clast		Ash-dense clast	Juxtaposing glassy and crystal-rich bands
Figures	Figure 8; Figure S3	Figure 9A	Figure 9B; Figure S4		Figure 10; Figure S5	Figure 11; Figure S6
Length scales of element variability in µm (calculated timescales)	Li 250		200 (15-120 s)		100 (1–4 min) 200 (2–4 min)	100 (5–10 s)
	Na					
	Rb		500 (4–16 hr)			100 (1–8 min)
	Cs	<50				
	Cu <500					
	Tl 300 (2–8 hr)	<50	500 (2–8 hr)			
	Pb <150 (60–100 hr)					
	In 500		200			
Comments	Only V4 has In variation. Li gradients are inconclusive and not discussed further with respect to nozzles.	Profile between one ash-filled bubble and one open bubble	Clast has dense ~200 µm-wide rim elevated in Li, K, Rb, Cs, Pb, Tl and Cl, and depleted in In and Bi, relative to plateau core concentrations.		Clast is banded but profile does not extend into a texturally different band.	A pumiceous band in a dense domain has depletions in Li, Zn, Rb, Cs and Pb and enrichment in Cu with respect to neighbouring bands (Tl and Bi data inconclusive).

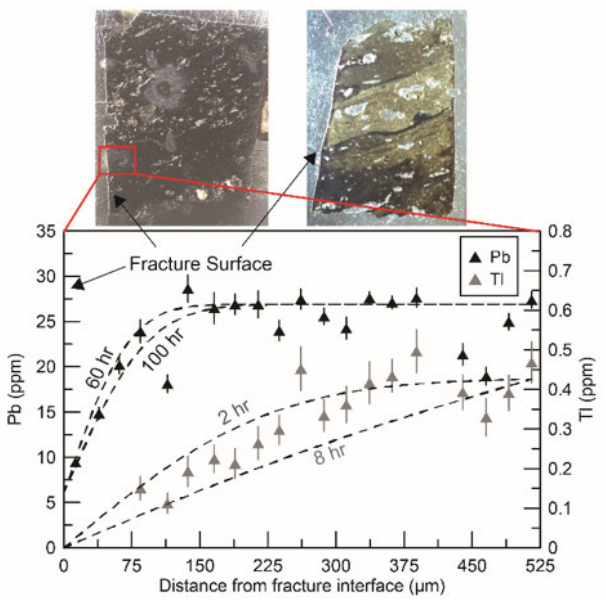

Figure 8: Pb and Tl elemental gradients away from a fracture surface in a nozzle (Sample V5) indicate the diffusion of volatile elements towards the fracture interface and partitioning into the fluxing vapour phase. Dashed lines are bounding timescales, calculated via an explicit finite-difference model, and constrain the timescale of gas fluxing between opening of pathway and cessation of gas fluxing. Errors bars are 2 Standard Error.

of the breccia in a subsequent explosive event. These timescales are comparable to those of sintering for the matrix ash shards given their size (~30 µm across) and the eruptive conditions [Castro et al. 2013; Giordano et al. 2008; Vasseur et al. 2013].

Third, the chemical and textural heterogeneity in V2 constrain the timing of multiple fracturing and degassing events this bomb underwent. At first the microcrystalline material, likely a nozzle host, underwent gas fluxing for hours as calculated by Tl (2–8 hours) and Rb (4–16 hours) diffusion (Figure 9B). Far-field Li concentrations for this clast (~18.5 ppm) are lower than the average for this sample (~30 ppm) and average for Cordón Caulle (~36 ppm). Li diffuses faster than Rb or Tl (Table 2) thus this first event likely resulted in the depletion of Li from this material. Fluxing ceased either due to cooling, and negligible elemental diffusion, or plugging of the nozzle. Calculated Li diffusion (seconds) records a second short-lived event, possibly related to the cessation of gas fluxing, forming the small Li diffusion profile prior to quenching (Figure 9B). A short event, on the order of seconds, would not be preserved by slower diffusing element such as Tl. A new sub-vent formed and gas streaming and heating occurred, preserved as the dense, oxidised clast rim. Elevated Li, Rb, Tl, Cs and Pb (relative to clast core concentrations, Figure 9B) suggests chemical re-equilibration with a fluxing gas phase and metal re-sorption within the narrow zone of reheated material. The narrow width of this rim suggests the process was

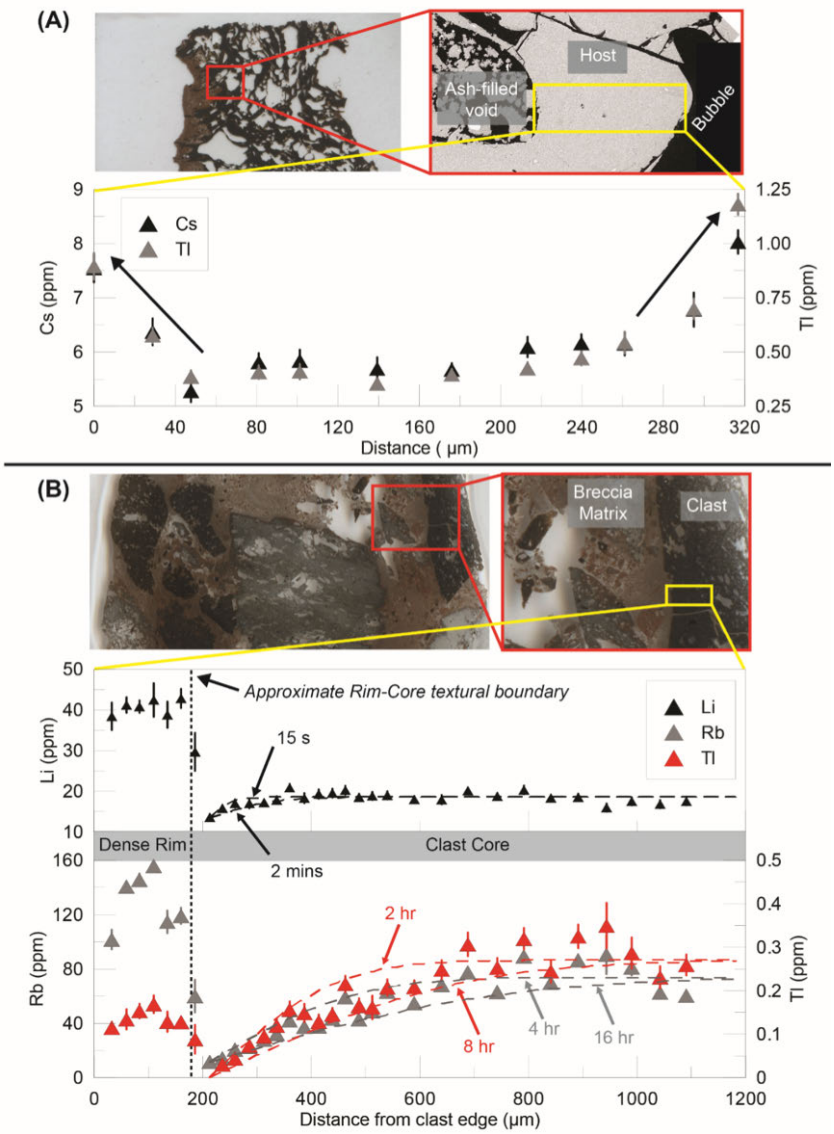

Figure 9: Elemental variations in oxidised, near-surface samples. [A] Cs and Tl concentrations are elevated at void-host interfaces in a vesiculated clast (Sample V1) due to potential late-stage resorption. [B] Observed Li, Rb and Tl element variations away from a matrix-clast interface in a dense clast (Sample V2) preserve the previous diffusion elements towards an open fracture induced by gas fluxing. Clast rim is chemically distinct from core. Dashed lines are bounding timescales, calculated via an explicit finite-difference model, and constrain the timescale between initiation and cessation of gas fluxing. Errors bars are 2 Standard Error.

short-lived and an explosive event formed the microcrystalline clast that preserves two periods of gas fluxing. This clast fell back into a new nozzle structure and is rapidly sintered to other clasts and before being re-ejected as the oxidised breccia bomb V2. The sintering of the ash matrix must have been fast as no clear diffusion profiles are recorded in the dense rim towards the clast interface or towards the depleted clast core. This clast exemplifies how repeating fracturing and degassing can progressively deplete melts and be recorded by elements that diffuse at different rates and have differing affinities for a gas phase.

Finally, Cu, Tl and Pb gradients are preserved away from fracture surfaces in nozzles where gas streaming occurred at the surface. Lead and Tl diffusion imply nozzles experience gas fluxing on the order of several hours to days (Figure 8). The discrepancy between the timescales calculated using Tl (2–8 hours) and Pb (60–100 hours) are due to uncertainties with model inputs. The trace element diffusion coefficients are calculated assuming a constant temperature, composition and melt viscosity throughout the eruption [Mungall 2002], this is a simplification of events but cannot be further constrained. As such, timescales are considered order of magnitude estimates of a single degassing process, rather than preserving two separate events. Schipper et al. [2013] observed individual ash jetting events occurring over timescales of seconds to tens of seconds

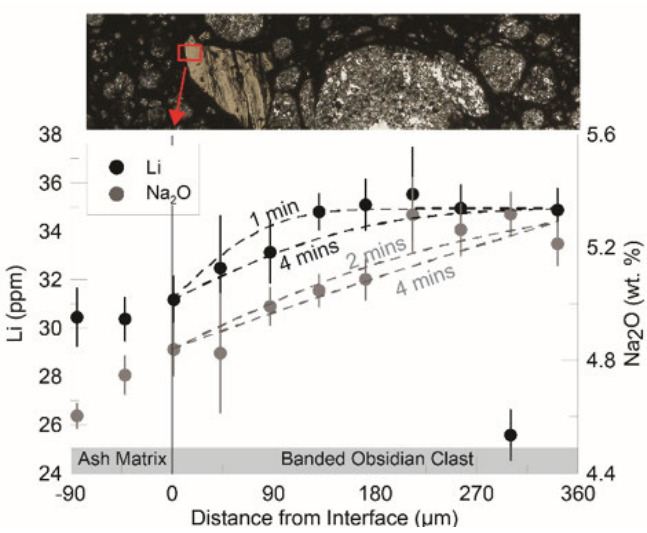

Figure 10: Li and Na elemental variation in a banded obsidian clast away from the matrix-clast interface in a non-oxidised pumice breccia (Sample B7) preserve the diffusion of alkalis into the gas phase fluxing (and carrying clasts) towards the surface. Dashed lines are bounding timescales, calculated via an explicit finite-difference model, and constrain the timescale between the fragmentation event that opened gas channel and cessation of gas fluxing due to sintering of matrix ash and secondary fragmentation event ejecting pumice breccia from the conduit. Errors bars are 2 Standard Error.

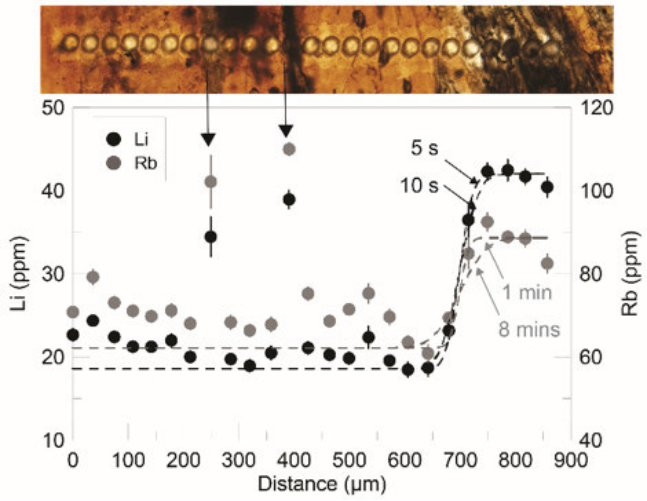

Figure 11: Li and Rb elemental variation across juxtaposed bands in a banded obsidian bomb (Sample B12) preserve the diffusion of alkalis between a high concentration and low concentration band. Dashed lines are bounding timescales, calculated via an explicit finite-difference model, and constrain the timescale between the two bands being juxtaposed and the bomb ejection and quenching event. Errors bars are 2 Standard Error.

during hybrid activity in January of 2012. However, sub-vents were long-lived, stable surface structures and repeated explosions were observed from the same locations over timescales of hours [Schipper et al. 2013]. Therefore, the hours-to-days timescales inferred from Pb, Tl and Rb heterogeneity in recycled nozzle material (clasts) and *in situ* sampled nozzles relate to the integration of numerous, ash jetting events from a single nozzle structure, rather than an individual event. Indeed, multiple ash jetting events would be expected to occur from any nozzle during its lifetime, prior to its rafting away from the locus of ash and gas venting, and cessation of elemental diffusion due to cooling. Our data are consistent with a persistent, more stable late vent structure that was connected with an extensive near-surface permeable network, allowing for protracted periods of outgassing.

Longer timescales later in the eruption likely relate to a better developed network of fractures that allow for more continuous gas fluxing throughout the conduit. This is consistent with observations from this eruption that show explosions progressively decreased in size with time [Schipper et al. 2013; Silva Parejas et al. 2012]. Pathways within the upper conduit being open for longer would facilitate this as extended periods of outgassing reduce overpressure within the system, thereby reducing the energy of explosions.

5.4 Summary: Fracturing Processes at Cordón Caulle

Figure 12 summarises the changing degassing processes with depth in the conduit and eruption duration, as well as the constrained timescales of certain degassing processes. Chemical and textural variation within the studied eruptive products are strongly linked and largely attributed to degassing-related processes. Alkali elements (Li, Rb, Cs) and certain metals (Cu, Tl, Pb, Bi) show the most systematic variability. Juxtaposed dense and pumiceous clasts in earlier-erupted breccia samples suggest fractures allow for extensive connectivity in the conduit during the early phases of the eruption, in line with the proposal that interconnected vesicles provided transient permeable degassing pathways in the upper ~1–1.5 km of the conduit [Schipper et al. 2013]. Timescales for fracturing, degassing and compaction of melt during the earlier explosive phases are short, on the order of minutes. These timescales indicate rapid and efficient degassing and sintering of melt prior to sudden bomb ejection and rapid quenching that preserves compositional heterogeneity. The short duration of these degassing events prevents their preservation in slower diffusing elements (e.g. Tl, Pb), with element variability largely confined to faster-diffusing alkali elements (e.g. Li). Matrix ash shards <30 µm across show depletions in elements such as Tl and Pb. The observation of repetitive Vulcanian explosions excavating the conduit during prolonged explosive activity fits with model predictions for regular pressure build-up and explosive events due to the high permeability threshold

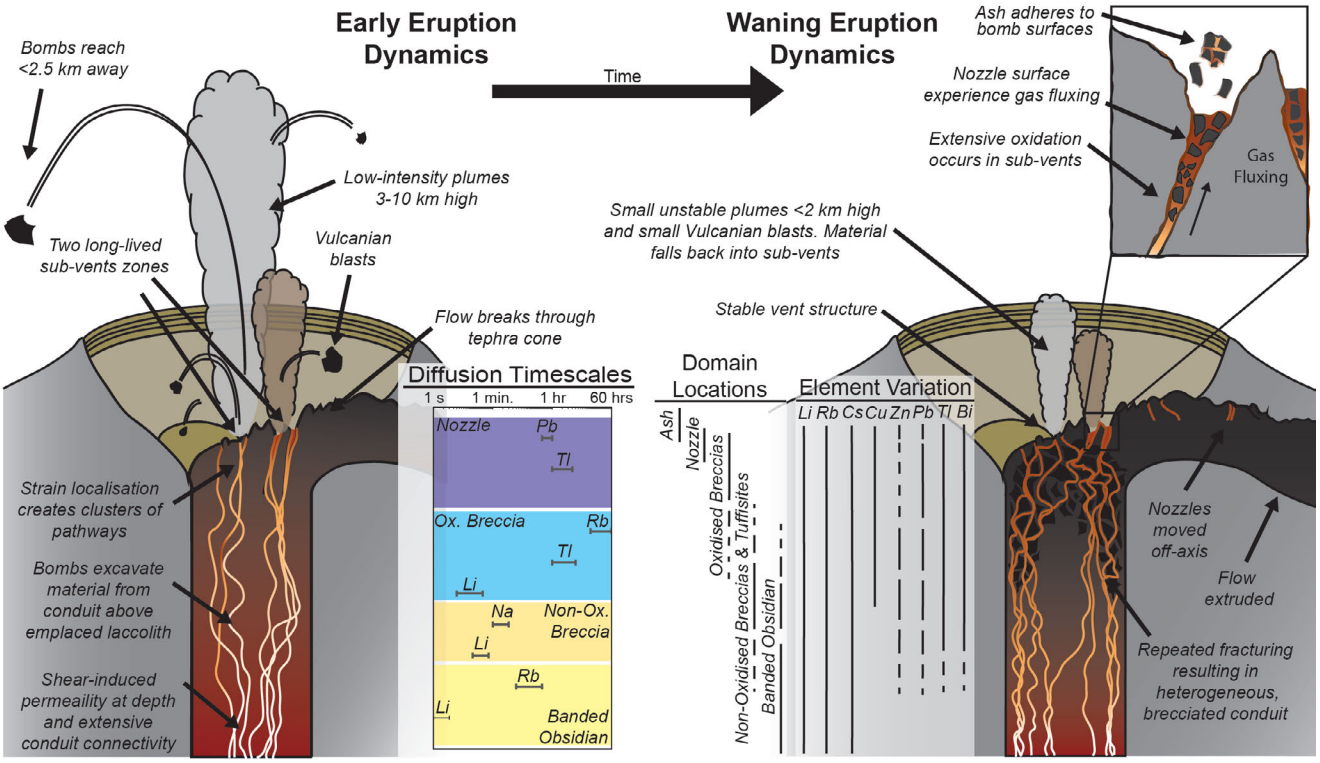

Figure 12: Summary figure highlighting how our chemical interpretations of the degassing processes throughout the eruption relate to observations summarised in Section 2. Early in the eruption degassing events are short-lived, and preserved largely by alkali elements, as large, repeating explosions excavate non-oxidised breccia and tuffisite-hosting bombs. Later in the eruption a more heterogeneous but stable vent structure allows for hours of gas fluxing from nozzles. Explosions eject oxidised breccia that chemically preserve many previous sub-surface fragmentation and degassing events. Longer periods of gas fluxing in the near-surface environment are preserved by a wider suite of metals (including Pb and Tl). Conduit is schematic and not to scale and represents the system above the emplaced laccolith described by Castro et al. [2016].

of the Cordón Caulle melt [Farquharson et al. 2017]. These conditions would also inhibit volatile exchange of fluxing gases with melt and prohibit the preservation of element enrichment that is seen in tuffisites in other systems [Berlo et al. 2013; Paisley et al. 2019]. Bomb excavation from this earlier phase (beginning June 7th and continuing into the hybrid activity phase beginning June 15th) was sufficiently deep to excavate material that had not undergone extensive oxidation by interactions with air, especially when compared to nozzle-sourced ejecta. Low H_2O concentrations indicate that *bombs* were probably sourced from above the level of laccolith emplaced 20-200 m below the surface [Castro et al. 2016; Pistolesi et al. 2015; Schipper et al. 2013; Silva Parejas et al. 2012].

The chemistry and textures of samples from later phases of the eruption (both *bomb* and *vent* samples) record an evolution in degassing systematics. *Vent* samples are more degassed than earlier *bombs* or *flow* material (highlighted by their lower median In, Tl, and Bi concentrations, Figure 3). Breccias from the near-surface environment chemically and texturally preserve several fracturing and degassing events. Chemically this is recorded as samples with wide interquartile ranges (Figure 3) and high % RSDs (Supplementary Material 1) of trace element concentrations, the result of averaging the chemically distinct domains samples are comprised of individual clasts have oxidised textures indicative of extensive, protracted interaction with the atmosphere that was not confined to the final sintering event prior to bomb ejection (Figure 2). Such samples are likely sourced from the top metres of the conduit where there is ample scope for atmospheric interactions. Gradients in multiple elements (Li, Rb, Cu, Tl, Pb) towards fracture interfaces (in breccia clasts and nozzles) indicate that degassing events later in the eruption and nearer the surface were longer in duration (~hours). This implies the upper conduit and vent structure was more stable later in the eruption, with sub-vents stable over hours to days [Schipper et al. 2013]. Our chemical observations do not reflect a single ash jetting event from a sub-vent but instead represent the integration of repeated venting over the total nozzle lifespan.

Tuffisite and breccia ash represent the most permeable pathways for gases in the conduit, in the form of

initially-open fracture pathways. Systematic depletions in metals (e.g. Zn, Tl, Pb) relative to their hosts imply metal scavenging from ash shards by the gas phase all the way from depth to the surface, potentially aided by shallow system Cl degassing [Churakov et al. 2000; Villemant et al. 2008; Zajacz et al. 2008]. Only once the ash and gases reach the surface environment do systematic Tl enrichment develops. This suggests an abrupt change in the gas capacity of Tl, which drove rapid Tl resorption into the available silicate melt (the ash particles). Bi enrichment throughout permeable zones could reflect volatile input from more mafic magmas [Guo and Audétat 2017]. It is unresolved whether Bi is adsorbed onto the edges of shards within veins, or is entering the rhyolite melt at depth.

6 Conclusions

Our study highlights how trace metals can record degassing of ascending silicic magma, and how chemical and textural heterogeneity in silicic eruptive products can be strongly correlated. The low H_2O contents in the 2011–2012 Cordón Caulle erupted products have previously limited our understanding of its degassing systematics [Castro et al. 2014]. However, by combining chemical species that diffuse slower than H_2O, we have been able to: (1) link chemical and textural heterogeneity to highlight pathways for preferential gas fluxing; (2) constrain timescales of the syn-eruptive degassing processes that form these complex textures; and (3) link these to observations of eruptive behaviour. Results shed new light on the complexity of conduit degassing processes during explosive and hybrid rhyolitic activity. Our study reinforces the value of trace elements as tracers of degassing, particularly in systems where more commonly-used species (H_2O, CO_2, halogens) are heavily depleted. Such an approach can be applied to other volcanic complexes to investigate sub-surface degassing in progressively brecciated and heterogeneous conduits.

Acknowledgements

We thank Alex Corgne, Nicolas Vergara Pontigo and Felipe Ignacio P. Gallardo for assistance in the field; Anna Jung and Vincent van Hinsberg for constructive analytical and instrument assistance at McGill; and Bruce Charlier, Luisa Ashworth, and Elliot Swallow for advice at Victoria University of Wellington. Further thanks are extended to John Stix and Jim Gardner for constructive comments on an earlier version of this manuscript. RP was supported by travel and research grants from the Mineralogical Association of Canada, the Geological Society of America, McGill University and the Society of Economic Geologists. This work is supported by an NSERC Discovery Grant to KB. HT is supported by a Royal Society University Research Fellowship and thanks LU Facilities staff for assistance. CIS is supported by a Victoria University of Wellington Research Development Fund.

Author contributions

Sample collection was conducted by RP, KB, CIS and HT over several field seasons. Sample preparation was conducted by RP. Probe analyses were conducted by RP and JW under supervision of CIS who processed the EPMA data. Laser analyses and data processing were conducted by RP. All model and figure preparation was undertaken by RP. All authors contributed to idea development and manuscript preparation.

Data availability

All data are provided in the tables or in the Supplementary Material provided alongside the online version of this article.

References

Alloway, B. V., N. J. G. Pearce, G. Villarosa, V. Outes, and P. I. Moreno (2015). "Multiple melt bodies fed the AD 2011 eruption of Puyehue-Cordón Caulle, Chile". *Scientific Reports* 5.1. doi: 10.1038/srep17589.

Bagnato, E., A. Aiuppa, A. Bertagnini, C. Bonadonna, R. Cioni, M. Pistolesi, M. Pedone, and A. Hoskuldsson (2013). "Scavenging of sulphur, halogens and trace metals by volcanic ash: The 2010 Eyjafjallajökull eruption". *Geochimica et Cosmochimica Acta* 103, pp. 138–160. doi: 10.1016/j.gca.2012.10.048.

Baker, R., M. Rehkämper, T. Hinkley, S. Nielsen, and J. Toutain (2009). "Investigation of thallium fluxes from subaerial volcanism—Implications for the present and past mass balance of thallium in the oceans". *Geochimica et Cosmochimica Acta* 73.20, pp. 6340–6359. doi: 10.1016/j.gca.2009.07.014.

Berlo, K., H. Tuffen, V. Smith, J. Castro, D. Pyle, T. Mather, and K. Geraki (2013). "Element variations in rhyolitic magma resulting from gas transport". *Geochimica et Cosmochimica Acta* 121, pp. 436–451. doi: 10.1016/j.gca.2013.07.032.

Bertin, D., L. E. Lara, D. Basualto, Á. Amigo, C. Cardona, L. Franco, F. Gil, and J. Lazo (2015). "High effusion rates of the Cordón Caulle 2011–2012 eruption (Southern Andes) and their relation with the quasi-harmonic tremor". *Geophysical Research Letters* 42.17, pp. 7054–7063. DOI: 10.1002/2015g1064624.

Cabrera, A., R. F. Weinberg, H. M. N. Wright, S. Zlotnik, and R. A. F. Cas (2011). "Melt fracturing and healing: A mechanism for degassing and origin of silicic obsidian". *Geology* 39.1, pp. 67–70. DOI: 10.1130/g31355.1.

Cashman, K. V. and R. S. J. Sparks (2013). "How volcanoes work: A 25 year perspective". *Geological Society of America Bulletin* 125.5-6, pp. 664–690. DOI: 10.1130/b30720.1.

Castro, J. M., I. N. Bindeman, H. Tuffen, and C. I. Schipper (2014). "Explosive origin of silicic lava: Textural andδD–H 2 O evidence for pyroclastic degassing during rhyolite effusion". *Earth and Planetary Science Letters* 405, pp. 52–61. DOI: 10.1016/j.epsl.2014.08.012.

Castro, J. M., B. Cordonnier, C. I. Schipper, H. Tuffen, T. S. Baumann, and Y. Feisel (2016). "Rapid laccolith intrusion driven by explosive volcanic eruption". *Nature Communications* 7.1. DOI: 10.1038/ncomms13585.

Castro, J. M., B. Cordonnier, H. Tuffen, M. J. Tobin, L. Puskar, M. C. Martin, and H. A. Bechtel (2012). "The role of melt-fracture degassing in defusing explosive rhyolite eruptions at volcán Chaitén". *Earth and Planetary Science Letters* 333-334, pp. 63–69. DOI: 10.1016/j.epsl.2012.04.024.

Castro, J. M., C. I. Schipper, S. P. Mueller, A. S. Militzer, A. Amigo, C. S. Parejas, and D. Jacob (2013). "Storage and eruption of near-liquidus rhyolite magma at Cordón Caulle, Chile". *Bulletin of Volcanology* 75.4. DOI: 10.1007/s00445-013-0702-9.

Churakov, S. V., S. I. Tkachenko, M. A. Korzhinskii, R. E. Bocharnikov, and K. I. Shmulovich (2000). "Evolution of composition of high-temperature fumarolic gases from Kudryavy volcano, Iturup, Kuril Islands: The thermodynamic modeling". *Geochemistry International* 38.5.

Collini, E., M. S. Osores, A. Folch, J. G. Viramonte, G. Villarosa, and G. Salmuni (2013). "Volcanic ash forecast during the June 2011 Cordón Caulle eruption". *Natural Hazards* 66.2, pp. 389–412. DOI: 10.1007/s11069-012-0492-y.

Crank, J. (1975). "The mathematics of diffusion". *Oxford Science Publications*, p. 32.

Daga, R., S. R. Guevara, D. G. Poire, and M. Arribére (2014). "Characterization of tephras dispersed by the recent eruptions of volcanoes Calbuco (1961), Chaitén (2008) and Cordón Caulle Complex (1960 and 2011), in Northern Patagonia". *Journal of South American Earth Sciences* 49, pp. 1–14. DOI: 10.1016/j.jsames.2013.10.006.

Delgado, F., M. E. Pritchard, D. Basualto, J. Lazo, L. Córdova, and L. E. Lara (2016). "Rapid reinflation following the 2011-2012 rhyodacite eruption at Cordón Caulle volcano (Southern Andes) imaged by InSAR: Evidence for magma reservoir refill". *Geophysical Research Letters* 43.18, pp. 9552–9562. DOI: 10.1002/2016g1070066.

Delmelle, P., M. Lambert, Y. Dufrêne, P. Gerin, and N. Óskarsson (2007). "Gas/aerosol–ash interaction in volcanic plumes: New insights from surface analyses of fine ash particles". *Earth and Planetary Science Letters* 259.1-2, pp. 159–170. DOI: 10.1016/j.epsl.2007.04.052.

Edmonds, M., D. Pyle, and C. Oppenheimer (2002). "HCl emissions at Soufrière Hills Volcano, Montserrat, West Indies, during a second phase of dome building: November 1999 to October 2000". *Bulletin of Volcanology* 64.1, pp. 21–30. DOI: 10.1007/s00445-001-0175-0.

Farquharson, J. I., M. J. Heap, Y. Lavallée, N. R. Varley, and P. Baud (2016). "Evidence for the development of permeability anisotropy in lava domes and volcanic conduits". *Journal of Volcanology and Geothermal Research* 323, pp. 163–185. DOI: 10.1016/j.jvolgeores.2016.05.007.

Farquharson, J. I., F. B. Wadsworth, M. J. Heap, and P. Baud (2017). "Time-dependent permeability evolution in compacting volcanic fracture systems and implications for gas overpressure". *Journal of Volcanology and Geothermal Research* 339, pp. 81–97. DOI: 10.1016/j.jvolgeores.2017.04.025.

Fick, A. (1855). "Ueber Diffusion". *Annalen der Physik und Chemie* 170.1, pp. 59–86. DOI: 10.1002/andp.18551700105.

Forte, P. and J. M. Castro (2019). "H2O-content and temperature limit the explosive potential of rhyolite magma during Plinian eruptions". *Earth and Planetary Science Letters* 506, pp. 157–167. DOI: 10.1016/j.epsl.2018.10.041.

Furukawa, K., K. Uno, and I. Miyagi (2010). "Mechanisms of oxidation and degassing in the Takanoobane rhyolite lava of Aso Volcano, Japan". *Journal of Volcanology and Geothermal Research* 198.3-4, pp. 348–354. DOI: 10.1016/j.jvolgeores.2010.09.015.

Gardner, J. E., K. S. Befus, J. Watkins, M. Hesse, and N. Miller (2012). "Compositional gradients surrounding spherulites in obsidian and their relationship to spherulite growth and lava cooling". *Bulletin of Volcanology* 74.8, pp. 1865–1879. DOI: 10.1007/s00445-012-0642-9.

Gardner, J. E., F. B. Wadsworth, E. W. Llewellin, J. M. Watkins, and J. P. Coumans (2018). "Experimental sintering of ash at conduit conditions and implications for the longevity of tuffisites". *Bulletin of Volcanology* 80.3. DOI: 10.1007/s00445-018-1202-8.

GeoReM (2009). *BCR-2G: GeoReM preferred values (1/2009)*. URL: http://georem.mpch-mainz.gwdg.de/sample_query_pref.asp (visited on 02/18/2011).

– (2015). *GeoReM: BCR-2G (published values)*. url: http://georem.mpch-mainz.gwdg.de/sample_query.asp (visited on 09/15/2015).

Gerlach, D. C., F. A. Frey, H. Moreno-Roa, and L. Lopez-Escobar (1988). "Recent volcanism in the Puyehue—Cordon Caulle region, Southern Andes, Chile (40· 5° S): petrogenesis of evolved lavas". *Journal of Petrology* 29.2, pp. 333–382. doi: 10.1093/petrology/29.2.333.

Giordano, D., J. K. Russell, and D. B. Dingwell (2008). "Viscosity of magmatic liquids: A model". *Earth and Planetary Science Letters* 271.1-4, pp. 123–134. doi: 10.1016/j.epsl.2008.03.038.

Gonnermann, H. M. and M. Manga (2003). "Explosive volcanism may not be an inevitable consequence of magma fragmentation". *Nature* 426.6965, pp. 432–435. doi: 10.1038/nature02138.

– (2005). "Flow banding in obsidian: A record of evolving textural heterogeneity during magma deformation". *Earth and Planetary Science Letters* 236.1-2, pp. 135–147. doi: 10.1016/j.epsl.2005.04.031.

Guo, H. and A. Audétat (2017). "Transfer of volatiles and metals from mafic to felsic magmas in composite magma chambers: An experimental study". *Geochimica et Cosmochimica Acta* 198, pp. 360–378. doi: 10.1016/j.gca.2016.11.029.

Heap, M., J. Farquharson, F. Wadsworth, S. Kolzenburg, and J. Russell (2015). "Timescales for permeability reduction and strength recovery in densifying magma". *Earth and Planetary Science Letters* 429, pp. 223–233. doi: 10.1016/j.epsl.2015.07.053.

Heiken, G., K. Wohletz, and J. Eichelberger (1988). "Fracture fillings and intrusive pyroclasts, Inyo Domes, California". *Journal of Geophysical Research: Solid Earth* 93.B5, pp. 4335–4350. doi: 10.1029/jb093ib05p04335.

Hinkley, T. K., M.-F. L. Cloarec, and G. Lambert (1994). "Fractionation of families of major, minor, and trace metals across the melt-vapor interface in volcanic exhalations". *Geochimica et Cosmochimica Acta* 58.15, pp. 3255–3263. doi: 10.1016/0016-7037(94)90053-1.

Isgett, S. J., B. F. Houghton, S. A. Fagents, S. Biass, A. Burgisser, and L. Arbaret (2017). "Eruptive and shallow conduit dynamics during Vulcanian explosions: insights from the Episode IV block field of the 1912 eruption of Novarupta, Alaska". *Bulletin of Volcanology* 79.8. doi: 10.1007/s00445-017-1138-4.

Jarosewich, E., J. Nelen, and J. A. Norberg (1980). "Reference Samples for Electron Microprobe Analysis". *Geostandards and Geoanalytical Research* 4.1, pp. 43–47. doi: 10.1111/j.1751-908x.1980.tb00273.x.

Jay, J., F. Costa, M. Pritchard, L. Lara, B. Singer, and J. Herrin (2014). "Locating magma reservoirs using InSAR and petrology before and during the 2011–2012 Cordón Caulle silicic eruption". *Earth and Planetary Science Letters* 395, pp. 254–266. doi: 10.1016/j.epsl.2014.03.046.

Jicha, B. R., B. S. Singer, B. L. Beard, C. M. Johnson, H. Moreno-Roa, and J. A. Naranjo (2007). "Rapid magma ascent and generation of 230Th excesses in the lower crust at Puyehue–Cordón Caulle, Southern Volcanic Zone, Chile". *Earth and Planetary Science Letters* 255.1-2, pp. 229–242. doi: 10.1016/j.epsl.2006.12.017.

Jochum, K. P., U. Weis, B. Stoll, D. Kuzmin, Q. Yang, I. Raczek, D. E. Jacob, A. Stracke, K. Birbaum, D. A. Frick, D. Günther, and J. Enzweiler (2011). "Determination of Reference Values for NIST SRM 610-617 Glasses Following ISO Guidelines". *Geostandards and Geoanalytical Research* 35.4, pp. 397–429. doi: 10.1111/j.1751-908x.2011.00120.x.

Kendrick, J. E., Y. Lavallée, N. R. Varley, F. B. Wadsworth, O. D. Lamb, and J. Vasseur (2016). "Blowing Off Steam: Tuffisite Formation As a Regulator for Lava Dome Eruptions". *Frontiers in Earth Science* 4. doi: 10.3389/feart.2016.00041.

Kolzenburg, S., M. J. Heap, Y. Lavallée, J. K. Russell, P. G. Meredith, and D. B. Dingwell (2012). "Strength and permeability recovery of tuffisite-bearing andesite". *Solid Earth* 3.2, pp. 191–198. doi: 10.5194/se-3-191-2012.

Kolzenburg, S. and J. K. Russell (2014). "Welding of pyroclastic conduit infill: A mechanism for cyclical explosive eruptions". *Journal of Geophysical Research: Solid Earth* 119.7, pp. 5305–5323. doi: 10.1002/2013jb010931.

Lara, L., J. Naranjo, and H. Moreno (2004). "Rhyodacitic fissure eruption in Southern Andes (Cordón Caulle 40.5°S) after the 1960 (Mw:9.5) Chilean earthquake: a structural interpretation". *Journal of Volcanology and Geothermal Research* 138.1-2, pp. 127–138. doi: 10.1016/j.jvolgeores.2004.06.009.

Lara, L. E., A. Lavenu, J. Cembrano, and C. Rodrıguez (2006). "Structural controls of volcanism in transversal chains: Resheared faults and neotectonics in the Cordón Caulle–Puyehue area (40.5°S), Southern Andes". *Journal of Volcanology and Geothermal Research* 158.1-2, pp. 70–86. doi: 10.1016/j.jvolgeores.2006.04.017.

Lowenstern, J. B., H. Bleick, J. A. Vazquez, J. M. Castro, and P. B. Larson (2012). "Degassing of Cl, F, Li, and Be during extrusion and crystallization of the rhyolite dome at Volcán Chaitén, Chile during 2008 and 2009". *Bulletin of Volcanology* 74.10, pp. 2303–2319. doi: 10.1007/s00445-012-0663-4.

MacKenzie, J. M. and D. Canil (2008). "Volatile heavy metal mobility in silicate liquids: Implications for volcanic degassing and eruption prediction". *Earth and Planetary Science Letters* 269.3-4, pp. 488–496. doi: 10.1016/j.epsl.2008.03.005.

Magnall, N., M. R. James, H. Tuffen, and C. Vye-Brown (2017). "Emplacing a Cooling-Limited Rhyolite Lava Flow: Similarities with Basaltic Lava Flows". *Frontiers in Earth Science* 5. doi: 10.3389/feart.2017.00044.

Magnall, N., M. R. James, H. Tuffen, C. Vye-Brown, C. I. Schipper, J. M. Castro, and A. G. Davies (2018). "The origin and evolution of breakouts in a cooling-limited rhyolite lava flow". *GSA Bulletin* 131.1-2, pp. 137–154. DOI: 10.1130/b31931.1.

Mather, T., M. Witt, D. Pyle, B. Quayle, A. Aiuppa, E. Bagnato, R. Martin, K. Sims, M. Edmonds, A. Sutton, and E. Ilyinskaya (2012). "Halogens and trace metal emissions from the ongoing 2008 summit eruption of Kılauea volcano, Hawai'i". *Geochimica et Cosmochimica Acta* 83, pp. 292–323. DOI: 10.1016/j.gca.2011.11.029.

Moriizumi, M., S. Nakashima, S. Okumura, and Y. Yamanoi (2009). "Color-change processes of a plinian pumice and experimental constraints of color-change kinetics in air of an obsidian". *Bulletin of Volcanology* 71.1, pp. 1–13. DOI: 10.1007/s00445-008-0202-5.

Moune, S., P.-J. Gauthier, S. R. Gislason, and O. Sigmarsson (2006). "Trace element degassing and enrichment in the eruptive plume of the 2000 eruption of Hekla volcano, Iceland". *Geochimica et Cosmochimica Acta* 70.2, pp. 461–479. DOI: 10.1016/j.gca.2005.09.011.

Mujin, M., M. Nakamura, and A. Miyake (2017). "Eruption style and crystal size distributions: Crystallization of groundmass nanolites in the 2011 Shinmoedake eruption". *American Mineralogist* 102.12, pp. 2367–2380. DOI: 10.2138/am-2017-6052ccbyncnd.

Mungall, J. E. (2002). "Empirical models relating viscosity and tracer diffusion in magmatic silicate melts". *Geochimica et Cosmochimica Acta* 66.1, pp. 125–143. DOI: 10.1016/s0016-7037(01)00736-0.

Paisley, R., K. Berlo, B. Ghaleb, and H. Tuffen (2019). "Geochemical constraints on the role of tuffisite veins in degassing at the 2008–09 Chaitén and 2011–12 Cordón Caulle rhyolite eruptions". *Journal of Volcanology and Geothermal Research* 380, pp. 80–93. DOI: 10.1016/j.jvolgeores.2019.05.013.

Pallister, J. S., A. K. Diefenbach, W. C. Burton, J. Muñoz, J. P. Griswold, L. E. Lara, J. B. Lowenstern, and C. E. Valenzuela (2013). "The Chaitén rhyolite lava dome: Eruption sequence, lava dome volumes, rapid effusion rates and source of the rhyolite magma". *Andean Geology* 40.2. DOI: 10.5027/andgeov40n2-a06.

Paton, C., J. Hellstrom, B. Paul, J. Woodhead, and J. Hergt (2011). "Iolite: Freeware for the visualisation and processing of mass spectrometric data". *Journal of Analytical Atomic Spectrometry* 26.12, p. 2508. DOI: 10.1039/c1ja10172b.

Pistolesi, M., R. Cioni, C. Bonadonna, M. Elissondo, V. Baumann, A. Bertagnini, L. Chiari, R. Gonzales, M. Rosi, and L. Francalanci (2015). "Complex dynamics of small-moderate volcanic events: the example of the 2011 rhyolitic Cordón Caulle eruption, Chile". *Bulletin of Volcanology* 77.1. DOI: 10.1007/s00445-014-0898-3.

Plail, M., M. Edmonds, M. C. Humphreys, J. Barclay, and R. A. Herd (2014). "Geochemical evidence for relict degassing pathways preserved in andesite". *Earth and Planetary Science Letters* 386, pp. 21–33. DOI: 10.1016/j.epsl.2013.10.044.

Pokrovski, G. S., A. Y. Borisova, and A. Y. Bychkov (2013). "Speciation and Transport of Metals and Metalloids in Geological Vapors". *Reviews in Mineralogy and Geochemistry* 76.1, pp. 165–218. DOI: 10.2138/rmg.2013.76.6.

Ruggieri, F., J.-L. Fernández-Turiel, J. Saavedra, D. Gimeno, E. Polanco, and J. A. Naranjo (2011). "Environmental geochemistry of recent volcanic ashes from the Southern Andes". *Environmental Chemistry* 8.3, p. 236. DOI: 10.1071/en10097.

Ruprecht, P. and H. Winslow (2017). "Short-circuiting magma differentiation from basalt straight to rhyolite?" *AGU Fall Meeting Abstracts*.

Saubin, E., H. Tuffen, L. Gurioli, J. Owen, J. M. Castro, K. Berlo, E. M. McGowan, C. I. Schipper, and K. Wehbe (2016). "Conduit Dynamics in Transitional Rhyolitic Activity Recorded by Tuffisite Vein Textures from the 2008–2009 Chaitén Eruption". *Frontiers in Earth Science* 4. DOI: 10.3389/feart.2016.00059.

Schipper, C. I., J. M. Castro, H. Tuffen, M. R. James, and P. How (2013). "Shallow vent architecture during hybrid explosive–effusive activity at Cordón Caulle (Chile, 2011–12): Evidence from direct observations and pyroclast textures". *Journal of Volcanology and Geothermal Research* 262, pp. 25–37. DOI: 10.1016/j.jvolgeores.2013.06.005.

Schipper, C. I., J. M. Castro, H. Tuffen, F. B. Wadsworth, D. Chappell, A. E. Pantoja, M. P. Simpson, and E. C. L. Ru (2015). "Cristobalite in the 2011–2012 Cordón Caulle eruption (Chile)". *Bulletin of Volcanology* 77.5. DOI: 10.1007/s00445-015-0925-z.

Schipper, C. I., J. Castro, B. Kennedy, B. Christenson, A. Aiuppa, B. Alloway, P. Forte, G. Seropian, and H. Tuffen (2019). "Halogen (Cl, F) release during explosive, effusive, and intrusive phases of the 2011 rhyolitic eruption at Cordón Caulle volcano (Chile)". *Volcanica* 2.1, pp. 73–90. DOI: 10.30909/vol.02.01.7390.

SERNAGEOMIN/OVDAS (2012). *Reporte de Actividad volcánica (RAV) Región de los Ríos*. URL: http://sitiohistorico.sernageomin.cl/reportesVolcanes/20121030112714945RAV_N379_Los-R%5C%C3%5C%ADos_14092012.pdf (visited on 11/14/2019).

Silva Parejas, C., L. Lara, D. Bertin, A. Amigo, and G. Orozco (2012). "The 2011–2012 eruption of Cordón Caulle volcano (Southern Andes): Evolution, crisis management and current hazards". *EGU General Assembly Conference Abstracts*. Vol. 14, p. 9382.

Singer, B. S., B. R. Jicha, M. A. Harper, J. A. Naranjo, L. E. Lara, and H. Moreno-Roa (2008). "Eruptive history, geochronology, and magmatic evolution of the Puyehue-Cordon Caulle volcanic complex, Chile". *Geological Society of America Bulletin* 120.5-6, pp. 599–618. doi: 10.1130/b26276.1.

Stasiuk, M. V., J. Barclay, M. R. Carroll, C. Jaupart, J. C. Ratté, R. S. J. Sparks, and S. R. Tait (1996). "Degassing during magma ascent in the Mule Creek vent (USA)". *Bulletin of Volcanology* 58.2-3, pp. 117–130. doi: 10.1007/s004450050130.

Symonds, R. B., W. I. Rose, M. H. Reed, F. E. Lichte, and D. L. Finnegan (1987). "Volatilization, transport and sublimation of metallic and non-metallic elements in high temperature gases at Merapi Volcano, Indonesia". *Geochimica et Cosmochimica Acta* 51.8, pp. 2083–2101. doi: 10.1016/0016-7037(87)90258-4.

Tuffen, H. and D. Dingwell (2005). "Fault textures in volcanic conduits: evidence for seismic trigger mechanisms during silicic eruptions". *Bulletin of Volcanology* 67.4, pp. 370–387. doi: 10.1007/s00445-004-0383-5.

Tuffen, H., D. B. Dingwell, and H. Pinkerton (2003). "Repeated fracture and healing of silicic magma generate flow banding and earthquakes?" *Geology* 31.12, p. 1089. doi: 10.1130/g19777.1.

Tuffen, H., M. R. James, J. M. Castro, and C. I. Schipper (2013). "Exceptional mobility of an advancing rhyolitic obsidian flow at Cordón Caulle volcano in Chile". *Nature Communications* 4.1. doi: 10.1038/ncomms3709.

Vasseur, J., F. B. Wadsworth, Y. Lavallée, K.-U. Hess, and D. B. Dingwell (2013). "Volcanic sintering: Timescales of viscous densification and strength recovery". *Geophysical Research Letters* 40.21, pp. 5658–5664. doi: 10.1002/2013gl058105.

Villemant, B., J. Mouatt, and A. Michel (2008). "Andesitic magma degassing investigated through H2O vapour–melt partitioning of halogens at Soufrière Hills Volcano, Montserrat (Lesser Antilles)". *Earth and Planetary Science Letters* 269.1-2, pp. 212–229. doi: 10.1016/j.epsl.2008.02.014.

Von Aulock, F. W., B. M. Kennedy, A. Maksimenko, F. B. Wadsworth, and Y. Lavallée (2017). "Outgassing from Open and Closed Magma Foams". *Frontiers in Earth Science* 5. doi: 10.3389/feart.2017.00046.

Wadsworth, F. B., J. Vasseur, B. Scheu, J. E. Kendrick, Y. Lavallée, and D. B. Dingwell (2016). "Universal scaling of fluid permeability during volcanic welding and sediment diagenesis". *Geology* 44.3, pp. 219–222. doi: 10.1130/g37559.1.

Wahrenberger, C. (2002). "Volatile trace-element transport in high-temperature gases from Kudriavy volcano (Itrup, Kurile Islands, Russia)". *Geochemical Society, Special Publications* 7, pp. 307–327.

Watkins, J., J. Gardner, and K. Befus (2017). "Nonequilibrium degassing, regassing, and vapor fluxing in magmatic feeder systems". *Geology* 45.2, pp. 183–186. doi: 10.1130/g38501.1.

Webster, J. D. (1990). "Partitioning of F between H2O and CO2 fluids and topaz rhyolite melt". *Contributions to Mineralogy and Petrology* 104.4, pp. 424–438. doi: 10.1007/bf01575620.

Williams-Jones, A. E., A. A. Migdisov, S. M. Archibald, and Z. Xiao (2002). "Vapor-transport of ore metals". *Water–Rock Interaction, Ore Deposits, and Environmental Geochemistry: A Tribute to David A. Crerar*. Ed. by R. Hellman and S. A. Wood. The Geochemical Society, pp. 279–306.

Wright, H. M. N., K. V. Cashman, M. Rosi, and R. Cioni (2007). "Breadcrust bombs as indicators of Vulcanian eruption dynamics at Guagua Pichincha volcano, Ecuador". *Bulletin of Volcanology* 69.3, pp. 281–300. doi: 10.1007/s00445-006-0073-6.

Zajacz, Z., W. E. Halter, T. Pettke, and M. Guillong (2008). "Determination of fluid/melt partition coefficients by LA-ICPMS analysis of co-existing fluid and silicate melt inclusions: Controls on element partitioning". *Geochimica et Cosmochimica Acta* 72.8, pp. 2169–2197. doi: 10.1016/j.gca.2008.01.034.

Zhang, Y. and H. Ni (2010). "Diffusion of H, C, and O Components in Silicate Melts". *Reviews in Mineralogy and Geochemistry* 72.1, pp. 171–225. doi: 10.2138/rmg.2010.72.5.

Zhang, Y., H. Ni, and Y. Chen (2010). "Diffusion Data in Silicate Melts". *Reviews in Mineralogy and Geochemistry* 72.1, pp. 311–408. doi: 10.2138/rmg.2010.72.8.